HHS Public Access

Author manuscript

Biofabrication. Author manuscript; available in PMC 2024 July 20.

Published in final edited form as:

Biofabrication. ; 15(4): . doi:10.1088/1758-5090/ace0db.

Gelatin Methacryloyl and Laponite bioink for 3D bioprinted Organotypic Tumor Modeling

Natan Roberto de Barros[1], **Alejandro Gomez**[1,2,3], **Menekse Ermis**[1,4], **Natashya Falcone**[1], **Reihaneh Haghniaz**[1], **Patric Young**[1], **Yaqi Gao**[1,2], **Albert-Fred Aquino**[3], **Siyuan Li**[1,2,5], **Siyi Niu**[1,2,6], **RunRun Chen**[1,2], **Shuyi Huang**[1,2], **Yangzhi Zhu**[1], **Payam Eliahoo**[7], **Arthur Sun**[1,2,9], **Danial Khorsandi**[1], **Jinjoo Kim**[1], **Jonathan Kelber**[3], **Ali Khademhosseini**[1], **Han-Jun Kim**[1,8], **Bingbing Li**[1,2]

[1]Terasaki Institute for Biomedical Innovation (TIBI), 1018 Westwood Blvd, Los Angeles, CA 90024, USA

[2]Autonomy Research Center for STEAHM (ARCS), California State University, Northridge, CA 91324, USA

[3]Department of Biology, California State University, Northridge, CA 91330, USA

[4]METU Center of Excellence in Biomaterials and Tissue Engineering, Middle East Technical University, Ankara 06800, Turkey

[5]Department of Biomedical Engineering, Wake Forest Institute for Regenerative Medicine, Winston-Salem, NC 27101, USA

[6]Department of Biology, University of California, Irvine, CA 92697, USA

[7]Department of Biomedical Engineering, University of Southern California, CA 90007, USA

[8]College of Pharmacy, Korea University, Sejong, 30019, Republic of Korea

[9]Department of Integrative Biology, University of California, Berkeley, CA 94720, USA

Abstract

Three-dimensional (3D) *in vitro* tumor models that can capture the pathophysiology of human tumors are essential for cancer biology and drug development. However, simulating the tumor microenvironment is still challenging because it consists of a heterogeneous mixture of various cellular components and biological factors. In this regard, current extracellular matrix (ECM)-mimicking hydrogels used in tumor tissue engineering lack physical interactions that can keep biological factors released by encapsulated cells within the hydrogel and improve paracrine interactions. Here, we developed a nanoengineered ion-covalent cross-linkable bioink to construct 3D bioprinted organotypic tumor models. The bioink was designed to implement the tumor ECM by creating an interpenetrating network composed of gelatin methacryloyl (GelMA), a light cross-linkable polymer, and synthetic nanosilicate (Laponite) that exhibits a unique ionic charge to improve retention of biological factors released by the encapsulated cells and assist

bingbing.li@csun.edu, hanjun@korea.ac.kr, and khademh@terasaki.org.

Conflict of Interest

The authors declare that they have no competing interests.

in paracrine signals. The physical properties related to printability were evaluated to analyze the effect of Laponite hydrogel on bioink. Low GelMA (5%) with high Laponite (2.5-3.5%) composite hydrogels and high GelMA (10%) with low Laponite (1.0-2.0%) composite hydrogels showed acceptable mechanical properties for 3D printing. However, a low GelMA composite hydrogel with a high Laponite content could not provide acceptable cell viability. Fluorescent cell labeling studies showed that as the proportion of Laponite increased, the cells became more aggregated to form larger 3D tumor structures. RT-qPCR and western blot experiments showed that an increase in the Laponite ratio induces upregulation of growth factor and tissue remodeling-related genes and proteins in tumor cells. In contrast, cell cycle and proliferation-related genes were downregulated. On the other hand, concerning fibroblasts, the increase in the Laponite ratio indicated an overall upregulation of the mesenchymal phenotype-related genes and proteins. Our study may provide a rationale for using Laponite-based hydrogels in 3D cancer modeling.

Keywords

3D Bioprinting; Gelatin Methacryloyl; Silicate nanoplatelet; Organotypic; Pancreatic Cancer; Nanoengineered composite hydrogel

1. Introduction

The tumor microenvironment (TME) is composed of a heterogeneous mixture containing a diverse spectrum of cellular components and biological factors [1, 2]. Cellular components constituting TME include cancer-associated fibroblasts (CAFs), macrophages (M1 or M2 phenotype), antigen-presenting cells, and effector cells, as well as tumor cells [1, 3]. In addition to the cellular components, various biological factors, such as the extracellular matrix (ECM) surrounding the cells and the cytokine/growth factor gradient, can affect TME [1, 4]. For decades, tremendous efforts have been made to mimic TME to elucidate tumor behavior and to discover drugs with optimal antitumor efficacy [5].

As part of these numerous efforts, biofabrication strategies are used to design 3D *in vitro* models that mimic the structure and function of tissues using ECM-mimicking biomaterials and cells constituting specific organs [6, 7]. In particular, 3D bioprinting technology is promising in tumor modeling because it can simulate pathophysiological phenomena with precise tissue structure and provide porosity, polarity, and gradient through ECM compositions [5, 8, 9]. However, since TME is composed of different cell types and a highly heterogeneous matrix/protein structure rather than single components/monostructures, there is an unmet need to establish more reliable tumor models using appropriate bioinks. In this regard, tumor modeling should consider the study of biological mechanisms that facilitate biological signalings, such as cytokine and growth factor-mediated communication within the scaffold, and the introduction of heterogeneous bioinks (*i.e.*, integrating stromal cells such as fibroblasts) to ensure the complexity of TME.

In this study, we developed a nanoengineered ion-covalent cross-linkable bioink containing both tumor cells (MIA PaCa-2, pancreatic cancer) and stromal cells (C3H10T1/2, fibroblast) to construct a 3D bioprinted organotypic tumor model. To this end, the bioink was designed to implement the ECM by creating an interpenetrating network composed of

gelatin methacryloyl (GelMA) with synthetic nanosilicate (Laponite) hydrogel. GelMA is a gelatin-based cross-linkable hydrogel and is a representative bioink used for 3D bioprinting [12]. The methacryloyl groups of GelMA allow for cross-linking of the matrix in the presence of photoinitiators and light irradiation [15], providing conformational fidelity and stability when cultured under physiological conditions [16]. GelMA also provides the RGD amino acid sequence (Arg-Gly-Asp) for integrin binding, which is advantageous for cell adhesion and survival [10]. However, GelMA alone does not keep a significant retention of biological factors released by the encapsulated cells to improve paracrine signaling within 3D scaffolds [11–13]. Furthermore, bioprinting of GelMA-based bioinks has been reported to be commonly performed at concentrations higher than 10% [14] or temperatures lower than 15°C; these printing conditions are employed primarily due to the relatively lower viscosity of GelMA solutions [15]. Nevertheless, increasing the concentration of the GelMA macromer not only increases the viscosity of the bioink but also increases the stiffness of the hydrogel, reducing the porosity required for cell spreading and proliferation [16].

Laponite, a synthetic silicate nanoplatelet, has been used as a rheological modifier and filler in food and cosmetic manufacturing [17]. Owing to their anisotropic superficial charges (edge: positive charges; surface: negative charges), Laponite can self-assemble (sheets, house of cards, dispersed) and interact with a variety of charged molecules [18]. It can form and dynamically break down these arrangements in aqueous solutions (shear-thinning properties) and be used as drug delivery and capturing systems [19, 20]. Recently, the unique characteristics of Laponite, including size, shape, charge distribution, and its shear-thinning properties due to a “house of card” structure formation, have been explored for potential use in biomedical fields [21–24]. In line with these efforts, we have reported various research results from endovascular hemorrhage control [25], embolism [26, 27], and drug delivery [28] using Laponite-based shear-thinning biomaterial. In particular, Laponite has been studied as a drug delivery scaffold due to its sustained release and pH-responsive release profile [28, 29]. In addition, as a bioink, Laponite has been studied mainly for simulating 3D modeling of bone and musculoskeletal systems [30–32]. Remarkably, Laponite has been shown to improve several biological processes, including protein targeting to membranes, responses to growth factors, morphogenesis associated with cell differentiation, and transforming growth factor (TGF)-β receptor signaling [33]. Due to Laponite’s physical, chemical, and biological properties discussed here, we hypothesized that utilizing Laponite in the composition of bioinks would improve the retention of released biological factors to improve paracrine signaling within encapsulated cells. In particular, despite these diverse biological possibilities, cancer modeling using Laponite hydrogel has not been elucidated to the best of the author’s knowledge. Adding Laponite to GelMA bioinks would provide bioinks with improved retention of biological factors released by the encapsulated cells, assist in paracrine signals for tumor tissue engineering, and improve shear-thinning properties for 3D bioprinting. A detailed schematic illustration of nanoengineered bioink is depicted in Fig. 1.

Here, we present a 3D bioprinted organotypic tumor model using a bioink incorporating multiple cell types (tumor cell, stromal cell) and a combination of GelMA and Laponite hydrogels. Eight compositional GelMA/Laponite bioinks were prepared and characterized regarding printability, rheological properties, compression stability, and porosity. Next, we

specifically modeled pancreatic cancer, which is known to have a pronounced stromal tissue involvement in tumor progression and prognosis [4]. Abundant desmoplastic matrix accumulation, one of the most striking hallmarks of pancreatic cancer, is a significant contributor to the inefficiency of anticancer therapies [34], with CAFs playing a role in this unique microenvironment [35].

The bioengineered organotypic 3D model was developed by incorporating human pancreatic carcinoma cells (MIA PaCa-2) and a mouse embryonic cell line that displays the morphology of fibroblasts and is functionally similar to mesenchymal stem cells (C3H10T1/2, Clone 8) as cancer and stromal components in a spatially defined 3D architecture.

Cell-laden GelMA/Laponite bioink was 3D bioprinted, followed by viability analysis. Live-cell labeling was used to assess the cellular distribution and morphology within the bioink. Furthermore, changes in biological response according to Laponite concentration were evaluated by detecting changes in mRNA and protein expression. The optimal printability of GelMA/Laponite-based bioink and the analysis of changes in the biological response of the tumor model according to Laponite concentration was presented. These studies can serve as a basis for the feasibility of 3D cancer modeling of Laponite-based hydrogels.

2. Materials and Methods

2.1. Materials and cells

2D nanoclay (Laponite) was purchased from (BYK Additives Ltd, TX, USA). Type A porcine skin gelatin, methacrylic anhydride, photoinitiator (PI) (2-hydroxy-4-(2-hydroxyethoxyethoxy)-2-methypropiophenone), formaldehyde solution (4% v/v), Triton X-100, and bovine serum albumin (BSA) were purchased from Sigma-Aldrich. To create a pancreatic cancer model, we have selected a pancreas carcinoma cell line (MIA PaCa-2, ATCC #CRL-1420™) and a mouse embryonic cell line that displays the morphology of fibroblasts and is functionally similar to mesenchymal stem cells [36–38] (C3H10T1/2, Clone 8, ATCC # CCL-226™). MIA PaCa-2 and C3H10T1/2 were cultured in Dulbecco's modified eagle medium (DMEM) supplemented with 10% fetal bovine serum (FBS) and 1% penicillin-streptomycin (ThermoFisher). Live&Dead cell viability kit, Alexa Fluor® 568 phalloidin, Dulbecco's phosphate-buffered saline (DPBS; GIBCO), CellTracker™ Red CMTPX Dye, and CellTracker™ Blue CMAC Dye were purchased from Thermo Fisher. Alexa Fluor® 647 Phalloidin was purchased from Cell Signaling Technology. The validated primers were obtained from Integrated DNA Technologies. UltraPure DNase/RNase Free water, and PowerUp SYBR Green Master Mix were purchased from Thermo Fisher. QuantiTect Reverse Transcription Kit was purchased from Qiagen.

2.2. GelMA synthesis

Gelatin methacryloyl was synthesized as described in previous studies [39, 40]. Briefly, type A porcine skin gelatin is diluted in DPBS at 60 °C and stirred continuously to reach a 10% w/v gelatin solution. Methacrylic anhydride is added to the gelatin solution (2:25 v/v) at a 0.5 ml/min rate and continuous stirring. After 1 h incubation, the reaction is stopped by

diluting with preheated DPBS (40 °C) and dialyzing against ultrapure water. The dialyzed solution is freeze-dried and stored at −20 °C until use. The GelMA solution is prepared by completely diluting the freeze-dried macromer with 0.5% (w/v) PI in DPBS.

2.3. Preparation of GelMA/Laponite composite bioinks

Stock solutions of 20% w/v GelMA (in DPBS) and 10% w/v Laponite (in ultrapure water) were used to prepare the GelMA/Laponite composite bioink. Composite bioinks of various concentrations of GelMA (5% and 10%) and Laponite (1.0%, 1.5%, 2.0%, 2.5%, 3.0%, and 3.5%) hydrogels were prepared from the stock solutions. GelMA hydrogel, Laponite hydrogel, and ultrapure water were put into a tube and mixed in a SpeedMixer (DAC 150.1 FVZ, FlackTek, USA) at 3000 rpm for 5 minutes. The mixing step was repeated 3 times with 5 min intervals between mixing. The bioinks were stored at 4 °C before use. Before any experimental procedures, the GelMA/Laponite composite bioinks were warmed at 37 °C for 30 minutes and equilibrated at 25 °C for 60 minutes.

2.4. Printing fidelity assessment

The printing fidelity of the GelMA/Laponite bioinks was assessed through the printing process performed on a BIO X bioprinter (CELLINK, USA) with a UV-protected cartridge connected to a polytetrafluoroethylene (PTFE) nozzle (30G), at 23 °C, 5 mm/s printing speed, and 50kPa to 80 kPa printing pressure. Monolayer structures were printed on polystyrene Petri dishes, and images were obtained to evaluate the printing fidelity in terms of fiber diameter. "D_r" stands for the fiber diameter ratio, "D_p" stands for the diameter of the printed fiber, and the PTFE nozzle diameter (D_n) is 370um. Based on the measured D_p values after 3D bioprinting, D_r is calculated according to the following calculation:

$$D_r = \frac{diameter\ of\ the\ printed\ fiber,\ D_p}{inner\ diameter\ of\ the\ nozzle,\ D_n}$$

The D_r is used to evaluate the deformation of printed fibers that achieve high printing fidelity when D_r is equal to or close to 1.

2.5. Injectability assessment of GelMA/Laponite composite bioinks

For injection force assessment, GelMA/Laponite bioinks were loaded into 3 cc syringes (BD Luer-Lok™ Syringe, # 309657) and injected through 30G PTFE nozzles (PTFE Dispensing Tip, #JG30-0.5TX). The bioinks were examined on a mechanical tester (Instron 5943, Instron Int. Ltd., MA, USA) using the Bluehill version 3 software with a 100 N load cell and an injection rate of 0.55 mm/s.

2.6. Rheological characterization

The rheological characteristics of GelMA/Laponite bioinks were assessed by a Rheometer (Anton Paar, MCR 302) following previous protocols [23]. Shear stress, viscosity, and storage moduli were evaluated with 25 mm sandblasted parallel-plate geometry. Oscillatory stress sweeps were recorded from 0.1 to 1000 Pa at 1 Hz.

2.7. Cell viability and metabolic activity assay

The effect of GelMA and Laponite on cellular viability was assessed. MIA PaCa-2 cells were loaded at a density of 2×10^6 cells/mL in the various compositions of GelMA/Laponite composite hydrogels. After 3D bioprinting, the samples were photo-crosslinked at 25 mW cm^{-2} for 60 s. The cell-laden photo-crosslinked scaffolds were cultured for up to 10 days. Live/Dead™ viability/cytotoxicity staining (Thermo Fischer Scientific, Waltham, MA, USA) was performed according to the manufacturer's protocol to visualize changes in cell viability within 3D bioprinted scaffolds. The fluorescence images (Calcein AM; green color: live cell/ Ethidium homodimer-1; red color: dead cell) were captured using a confocal microscope (Zeiss LSM 710, Germany).

In addition, a PrestoBlue™ cell viability reagent (Thermo Fischer Scientific, Waltham, MA, USA) was used to measure the relative metabolic activity of the cells encapsulated within the 3D bioprinted scaffolds. The fluorescence intensity (excitation: 560 nm; emission: 590 nm) was measured using a microplate reader (Varioskan LUX, ThermoFisher).

2.8. Pancreatic organotypic 3D microtumor

The GelMA/Laponite bioinks were utilized to fabricate a pancreatic tumor organotypic 3D microtumor. MIA PaCa-2, a human pancreatic cancer cell line, and C3H10T1/2, a mouse embryonic mesenchymal cell line, were mixed with the GelMA/Laponite composite bioinks at a density of 10^7 cells/ml (MIA PaCa-2:C3H10T1/2 = 1:1). The cell-laden bioinks were then bioprinted into PDMS-coated 48-well plates using a 3D bioprinter equipped with a temperature-controlled pneumatic printhead at 23 °C. Afterward, 3D bioprinted structures were UV cross-linked at 25 mW cm^{-2} for 60 s. The 3D bioprinted models were cultured for up to 14 days with cell culture media replenishment every 2 days. Cancer cells (Blue CellTracker) and fibroblasts (Red CellTracker) were labeled using live cell trackers to evaluate the distribution of each cellular component within the pancreatic organoid 3D microtumor model.

2.9. Quantitative Real-Time PCR analysis

3D microtumor constructs were cultured for 3 days and collected for gene expression analysis. G10L0 was used as a control. Total RNA was isolated and purified using the RNeasy® Plus Mini Kit (Qiagen, CA, USA). The QuantiTect Reverse Transcription Kit was used to transcribe total RNA into the cDNA. The gene expression level was analyzed by quantitative real-time polymerase chain reaction (RT-PCR) in a Bio-Rad CFX384 Real-Time PCR Detection System. PCR cycle conditions are as follows: initial denaturation, 5 min at 95 °C; recurring denaturation, 5 s at 95 °C; amplification, 10 s at 60 °C for 45 cycles. The relative expression level of all the mRNA was calculated and expressed as fold changes of the threshold cycle (Ct) using the $2^{-\Delta\Delta Ct}$ method. The average value of reference genes, including glyceraldehyde 3-phosphate dehydrogenase (GAPDH), beta-actin (β-actin), 18s ribosomal RNA (18s rRNA), and hypoxanthine phosphoribosyltransferase 1(HPRT1) was used for the normalization. The primer sequences of the targeted genes are displayed in Table S1.

2.10. Western Blot

Total protein was isolated from 3D microtumor constructs that had been incubated for three days. The M-PER extraction buffer (Thermo Fisher Scientific), supplemented with Halt phosphatase protease inhibitor (Thermo Fisher Scientific), was used to extract the protein. Protein concentration was determined via a Bradford Assay (Bio-Rad). Total protein (30 μg) was loaded on the 4-20% Mini-Protean gradient gel (Bio-Rad), and SDS-PAGE was performed. The separated proteins were transferred to PVDF membranes. The membranes were washed and blocked with 3% bovine serum albumin overnight at 4°C degree.
Then the membranes were incubated with antibodies for immunoblot analysis: anti-VEGF mouse antibody (Santa Cruz Biotechnology, 1:200), anti-Vimentin rabbit antibody (Abcam 1:1000), anti-IGF1 rabbit antibody (Abcam 1:1000), anti-TGFβ1 rabbit antibody (Abcam 1:1000), anti-β-Actin rabbit antibody (Cell Signaling Technology, 1:1000). Anti-mouse IgG (Cell Signaling Technology) and anti-rabbit IgG (Cell Signaling Technology) secondary antibodies were used at 1:2,000 dilutions. The membranes were then washed with TBS/T before being treated with a chemiluminescent substrate (ClarityTM Western ECL Substrate; Bio-Rad). The images of the membranes were taken using Azure Biosystems c500 Gel Imaging System, and the band intensities were quantified using Fiji software. Pixel intensity was measured from boxes around the bands of interest. The ratios of protein of interest to housekeeping protein were calculated and plotted.

2.11. Statistical Analysis

All data are presented as the mean ± standard error of the mean or standard deviation, as indicated in the figure captions. One-way or two-way ANOVA with Tukey's post-hoc analysis was conducted, as indicated in the text or figure captions. A p-value below 0.05 was regarded as statistically significant. Statistical significance was defined as $*p < 0.05$, $**p < 0.01$.

3. Results and Discussion

3.1. Printability assessment of GelMA/Laponite composite hydrogels

In the extrusion-based bioprinting process, it is well-known that inner nozzle diameter, pressure, printing speed, temperature, and bioink composition are parameters that can control and influence the morphology of printed fibers [41–43]. As a first step in optimizing the bioprinting process, we set the nozzle gauge (30G), temperature (23 °C), and printing speed (5 mm/s). We changed the GelMA/Laponite hydrogel compositions with controlled printing pressure (50kPa to 80 kPa). Single-layer structures were printed on polystyrene Petri dishes and imaged under a light microscope to assess the effect of the hydrogel composition on printing fidelity (Fig. 2A). As shown in Fig. 2B, as the ratio of Laponite increased, the overall thickness and shape of the printed GelMA/Laponite fibers were constant. Next, we evaluated the printability of composite hydrogels at a percentage range of 0.0-3.5% of Laponite in two GelMA percentages (5, 10%) (Fig. 2C). In the composite hydrogel, when the GelMA percentage was low (5%), and the Laponite content was less than 2.0%, the viscosity was too low to maintain the geometry. On the other hand, when the percentage of GelMA was high (10%) and the percentage of Laponite exceeded 2.5%, the viscosity was too high for extrusion. Based on these results, we divided into low GelMA %

(5%) with high Laponite % (2.5-3.5%) group and high GelMA % (10%) with low Laponite % (1.0-2.0%) group. A total of 8 hydrogel conditions were subsequently tested with the GelMA-only groups (5%, 10%). The printing fidelity was evaluated by determining the diameter ratio of printed fiber (D_p) to the nozzle diameter (D_d) (*i.e.*, fiber diameter ratio, D_r) (Fig. 2D). The control groups (GelMA 5% and 10%) were too liquid to form fibers during the printing process. Due to the relatively low viscosity and storage modulus, 5% GelMA composite hydrogels (G5Lx groups: G5L2.5, G5L3.0, G5L3.5) showed a larger diameter ratio (D_r) compared to the 10% GelMA composite hydrogels (G10Ly groups: G10L1.0, G10L1.5, G10L2.0).

3D structures were printed with different geometries using G10L1.5 composite hydrogel to qualitatively demonstrate the capability of printing multiple layers in various geometries. After the printing process, the 3D structures were UV light cross-linked (Fig. 2E) and stained with food dyes diluted in DPBS before being imaged (Fig. 2F). The composite hydrogel was able to maintain its structure after the printing process in a 2-layer grid model (green), an 8-layer tube model (blue), and a 3-layer honeycomb model (red). These results show that the GelMA composite hydrogel with Laponite is capable of multilayered bioprinting.

Laponite has the potential to have distinct beneficial effects on the printability of hydrogels in 3D bioprinting. Clay nanomaterials to which Laponite belongs have been reported to modulate and manipulate physical and chemical characteristics in polymeric systems, such as flow behavior, stiffness, swelling, and degradation [16]. For instance, compositing synthetic inorganic nanosilicates with bio or synthetic polymers generates complex electrostatic interactions between them and forms an internal organization within the solution [44, 45]. This process allows nanosilicates such as Laponite to increase shear-thinning and self-healing properties in polymer systems [46, 47]. These material characteristics of Laponite can have a positive effect on the 3D bioprinting field, as shown in our results.

3.2. Injectability and rheological evaluation of non-crosslinked GelMA/Laponite composite hydrogels

We analyzed the mechanical properties of GelMA/Laponite composite hydrogels before and after UV cross-link. First, a syringe loaded with an uncrosslinked composite hydrogel was set up, as shown in Fig. 3A, to measure the injection force. Generally, bioinks with improved injection forces are preferred due to their high viscosity and shape fidelity, which can improve 3D bioprinting outcomes [48]. The composite bioink group (G5L0, G5L2.5, G5L3.0, G5L3.5) containing 5% GelMA showed a low injection force with the 30G PTFE nozzle/3cc combination even at a high concentration of Laponite (3.5% w/v) according to the injectability evaluation. The maximum force required to inject the composite hydrogel G5L3.5 (GelMA 5%/Laponite 3.5%) through the syringe was observed to be about 6.7 N (Fig. 3B). We also tested another set of composite hydrogels containing 10% GelMA and low concentrations of Laponite (G10L0, G10L1.0, G10L1.5, G10L2.0) (Fig. 3C). As expected, even at lower Laponite concentrations (1%, 1.5%, and 2%), the composite hydrogel containing 10% GelMA had a higher injection force (8.21, 15.62, and 20.11

N, respectively) compared to the G5L3.5 composite hydrogel. An increasing, plateaued injection force curve with no clogging or non-uniform changes was shown irrespective of the composition of the hydrogel, suggesting that all composite bioinks exhibited a homogeneous quality. On the other hand, GelMA 5% without Laponite (G5L0) showed an injection force curve with a plateau level lower than the initial injection force required to remove the syringe piston from inertia, which is commonly observed in low viscosity compositions.

We evaluated the shear-thinning properties of the GelMA/Laponite composite hydrogels to investigate whether the composite hydrogels exhibit improved rheological properties over GelMA hydrogels (Fig. 3D). The shear-thinning behavior is an essential feature in extrusion 3D bioprinting, highlighting the self-assembly interactions between polymer and Laponite, that can be dynamically formed and destroyed [49, 50]. All composite hydrogels, except pure GelMA hydrogels (GelMA 5% and 10%), displayed progressively declining viscosity-strain curves on logarithmic scales (Fig. 3E and 3F), indicating shear-thinning behavior. In addition, the composite hydrogels showed self-healing behavior under cyclic oscillatory conditions, recovering to their initial modulus after various cycles. These results showed that GelMA/Laponite composite hydrogels acquire the typical characteristics of shear-thinning hydrogels by adding Laponite hydrogel. The initial rheological properties of the bioink are improved with increasing concentrations of GelMA and Laponite. Remarkably, increasing the Laponite fraction over the GelMA fraction significantly affects shear strength, viscosity, and self-healing properties. These rheological characteristics of our composite hydrogels are known to be due to the ionic Laponite-Laponite interactions in addition to GelMA-Laponite non-covalent surface interactions [51].

Furthermore, the rheological changes were analyzed during UV cross-linking of GelMA/Laponite composite hydrogel (Supplementary Fig. 1). All GelMA/Laponite composite hydrogels showed a cross-linking reaction plateau within 180-300 seconds. The difference in the cross-linking reaction time (reaction time: 10% > 5%) is due to the amount of GelMA in the composite hydrogel, while the Laponite effect on the cross-linking reaction time was not significant. The storage modulus (G') of the fully cross-linked G5Lx and G10Ly groups was evaluated as a function of the angular frequency (ω) to investigate the effect of Laponite on the mechanical behavior in the non-destructive strain range of the cross-linked composite hydrogel (Supplementary Fig. 1Bii and Cii). Laponite at a 2.5–3.5% concentration in the G5Lx group showed a storage modulus increase of at least 10 times. In the G10Ly group, Laponite at a 1.0–2.0% concentration showed a storage modulus increase of less than 10 times. This difference in storage modulus according to the concentration range of Laponite may be due to the unique phase characteristics of Laponite. Previous studies of the phase diagrams of Laponite have shown that up to a concentration of 2% (w/w), Laponite forms an isotropic liquid that is completely exfoliated but does not interact with each other [19, 44, 52–55]. However, at 2–3% (w/w) concentrations, Laponite forms isotropic gels with Laponite partially interacting with each other in a “house of cards” assembly. When the Laponite concentration exceeds 3% (w/w), Laponite becomes liquid crystals characterized by tightly packed “house of cards” assemblies with negligible Laponite movement [19, 53, 55]. Based on these previously reported studies, our results may indicate a dramatic storage

modulus increase in the G5Lx group with a Laponite ratio greater than 2% than in the G10Ly group with a Laponite ratio less than 2% in GelMA/Laponite composite hydrogel.

In biodegradability tests, the composite hydrogel of the G5Lx group containing 2.5% or more of Laponite did not degrade for more than 5 days, and the structure was maintained (Supplementary Fig. 2A). However, the G10Ly group containing less than 2% Laponite showed steady degradation for 5 days (Supplementary Fig. 2B). Interestingly, the GelMA alone group (G5L0, G10L0) was degraded within 1 day. In contrast, the *in vitro* degradation rate decreased as the concentration increased in the 1.0–2.5% Laponite range. These results show that the *in vitro* degradation of GelMA/Laponite hydrogels depends on Laponite rather than GelMA.

Furthermore, in microstructure analyses evaluated through scanning electron microscopy (SEM) (Supplementary Fig. 2C), the G5Lx groups showed an increased porous network than the G10Ly groups. The porous structure of the G5Lx group was amorphous and had various sizes. In contrast, the porous structure of the G10Ly group showed a more homogenous porous structure. However, the change in the porous structure according to the increase of the Laponite content was not significant. This result indicates that the porosity change of the composite hydrogel is due to gelatin-based polymer rather than Laponite, similar to the previous study [23]. In the previous study from our group, the porous network of shear-thinning hydrogels composed of Laponite and gelatin was mainly affected by gelatin rather than Laponite. It is also consistent with the results of another research group that the addition of Laponite did not significantly affect the porous structure [56]. Our mechanical testing results suggest that GelMA in GelMA/Laponite composite hydrogel affects microtissue stiffness and porous microstructure. On the other hand, adding Laponite is expected to cause shear thinning properties based on improved storage modulus required for 3D printing and delayed biodegradation.

3.3. *In vitro* biocompatibility assessment of cell-laden GelMA/Laponite composite bioinks

To develop a co-culture of cancer cells and stromal cells as an organotypic tumor model, we 3D bioprinted a pancreatic tumor model using GelMA/Laponite composite hydrogels containing both tumor cells and stromal cells. First, we analyzed whether cells encapsulated in GelMA/Laponite composite hydrogel of various compositions (G5Lx, G10Ly) exhibit adequate cell viability after 3D bioprinting. The viability of MIA PaCa-2 cells encapsulated in 3D bioprinted scaffolds was investigated by measuring Live/Dead cell staining (direct viability) and metabolic activity (indirect mitochondria activity) after culture for up to 7 and 10 days, respectively (Fig. 4).

The *in vitro* 3D reconstruction images confirmed differences in cell proliferation between the composite hydrogel groups. However, viable cells were observed in all groups (green labeling) (Fig. 4A and B). The G5Lx groups with high Laponite contents (G5L2.5, G5L3.0, G5L3.5) had relatively fewer viable cells than the G10Ly groups with low Laponite contents (G10L1.0, G10L1.5, G10L2.0). Notably, cells in the G10Ly group continued proliferating within the 3D bioprinted structures for up to 7 days to form cell aggregates (Supplementary Fig. 3A). In contrast, the G5Lx group had fewer cells, and it was distributed in a scattered and discrete pattern. Proliferation results in Supplementary Fig. 3 support observations

from Live/Dead cell staining. Because the electrostatic interaction of the Laponite-based hydrogel is capable of binding with ethidium homodimer-1 (red), the composite hydrogels were locally stained red (without nuclei morphology), which is consistent with published literature [57]. In particular, this trend was more pronounced as the concentration of Laponite in the gel increased, making it challenging to detect dead cells.

For quantitative analysis of cell viability (Fig. 4C–D) and proliferation (Supplementary Fig. 3), the experimental groups were cultured for 10 days. Mitochondrial activity was analyzed by PrestoBlue assay. As observed in the live/dead assay, the G5Lx group containing 2.5% or more of Laponite showed lower cell viability (less than 45% cell viability of control) than the G10Ly group containing 2% or less of Laponite (over 75% cell viability of control). In particular, there was no significant difference in cell viability between the G5L0 and G10L0 groups that did not contain Laponite (specific values at day 7: 285.74±48.07 G5L0; 242.24±13.71 G10L0). Hence, an increase in the amount of GelMA within the 5–10% range did not significantly affect cell viability. However, in Laponite above 2.5%, a decrease in cell viability was observed as the amount of Laponite increased.

Compared to previously reported findings, the concentration at which Laponite can affect cell growth may vary depending on the cell type. A previous study showed that NIH/3T3 fibroblasts cultured in the presence of 4.5% Laponite maintained cell viability for up to 14 days [23]. Another study reported that cell proliferation was not inhibited when human mesenchymal stem cells (MSCs) were encapsulated in 2% Laponite and cultured for 24 hours [58]. In addition, it has been reported that a 6% Laponite-based bioink can be used to 3D bioprint a mouse progenitor osteoblast line and maintain adequate viability for up to 7 days [49]. In these reports, Laponite hydrogels maintained cell viability at higher concentrations of Laponite in mesenchymal-originated cells than those tested with epithelial cells. In particular, due to their affinity for mesenchymal cells, Laponite-based scaffolds have been mainly proposed for use as bioinks for bone tissue engineering [31, 49, 59]. In our results, when encapsulating human pancreatic cancer cells using GelMA/Laponite composite hydrogel, biocompatibility could be maintained in the Laponite concentration range of less than 2% w/w, so the subsequent study was conducted using only the G10Ly groups.

3.4. *In vitro* cell morphology assessment of cell-laden GelMA/Laponite composite bioinks

Our fluorescence live/dead images showed that when Laponite was added to the G10Ly group, cell aggregation was observed depending on the proportion of Laponite (Fig. 4A). Purwada *et al.* reported similar observations when Laponite-based hydrogels were used to engineer *ex vivo* B cell follicles [60]. The authors demonstrate that Laponite can confer structural and signaling cues comparable to the lymphocyte microenvironment, facilitating a germinal center-like response. Based on this biological cue of Laponite, we analyzed the effects of GelMA/Laponite composites on cell fate, morphology, proliferation, and aggregation in a 3D bioprinted tumor model.

To better understand the effect of Laponite concentration on pancreatic cancer cells, MIA PaCa-2 cells at a density of 2×10^6 cells/mL were encapsulated in GelMA/Laponite composite hydrogels (G10Ly groups). 3D bioprinted microtumors were cultured for up to

14 days and stained with Lamin A/C antibody (nuclei, cyan) and Phalloidin (cytoskeleton, yellow) (Fig. 4E). Fluorescence image analysis showed that in the case of G10L0, pancreatic cancer cells tended to migrate towards the surface of the microtumor. In contrast, for G10L1.0 and G10L1.5, pancreatic cancer cells tend to form cell aggregates/spheroids (microaggregates) within the microtumor. However, when the Laponite concentration was further increased to 2% (G10L2.0), the cell aggregates became distinct (macroaggregate) and more widely distributed to fill the microtumors.

3.5. High-throughput fabrication of 3D bioprinted pancreatic cancer model using GelMA/Laponite composite bioink

In pancreatic cancer, 80% of the total volume of the tumor is derived from the stromal tissue (desmoplastic feature), and fibroblasts and CAFs play an important role in this unique microenvironment [34, 61]. CAFs support tumor progression and phenotypic transitions through paracrine signaling by secreted growth factors and interleukins [62–64]. In particular, CAFs and tumor cell interactions significantly impact overall tumor prognosis. For example, in an anticancer immunotherapeutic study, it has been reported that culturing 3D spheroids composed of pancreatic cancer cells and fibroblasts with monocytes promotes M2 phenotypic differentiation of monocytes and affects therapeutic efficacy [65]. In another study, CAF-activated pancreatic cancer cells increased cancer invasion by remodeling the metabolic conversion mechanisms, including the matrix metalloproteinase (MMP) pathways [66]. Therefore, it is essential to consider the influence of cellular and stromal factors, including fibroblasts, when developing an *in vitro* 3D tumor model that reflects cancer biology.

To meet these biological considerations, we co-encapsulated pancreatic cancer cells (MIA PaCa-2) and fibroblasts (C3H10T1/2) into the G10Ly composite hydrogels to fabricate 3D bioprinted organotypic microtumor models. Here, the bioprinter was utilized for high reproducibility and high-throughput fabrication of pancreatic cancer models.

This approach of high-throughput bioprinting of GelMA/Laponite composite hydrogel droplets encapsulating pancreatic cancer cells in co-culture with fibroblasts allowed us to minimize the complexity of the model and ensure volume and cell density in a high-precision manner. By bioprinting droplets, we were able to achieve several advantages that are crucial for our research goals. Firstly, this approach allowed us to minimize the complexity of the model, ensuring a more streamlined and efficient process. It enabled us to focus primarily on the biological aspects and interactions within the tumor microenvironment, which is essential for understanding PDAC progression and developing potential treatments.

Furthermore, by bioprinting droplets, we could precisely control the volume and cell density within each droplet. This high-precision deposition ensured consistent and reproducible experimental conditions, enabling us to study PDAC cell-fibroblast interactions and hydrogel composition affecting tumor behavior and activation of fibroblasts into CAFs in a controlled manner. The ability to manipulate these parameters is crucial for understanding the behavior of PDAC cells and their responses to various stimuli. Additionally, the high-throughput nature of droplet bioprinting allowed us to generate a large number of

PDAC tumor models in a relatively short time. This scalability is particularly important for screening potential therapeutic agents or testing different experimental conditions, ultimately contributing to accelerating research progress in the field.

For that, pancreatic cancer cells and fibroblasts were mixed in G10Ly bioinks in a 1:1 ratio and then 3D bioprinted in a 48-well plate (Fig. 5A, B). First, the total cellular viability and proliferation of the 3D microtumor were analyzed through Live/Dead viability assays (Fig. 5C) and PrestoBlue metabolic activity assay (Fig. 5D). Similar to the 3D microtumor results using only MIA PaCa-2 cells (Fig. 4C), the co-culture 3D microtumor samples did not show significant cytotoxicity at Laponite content below 2% (Supplementary Fig. 4). In z-stack image analysis, cells were highly packed into a 3D microtissue with a green fluorescence signal (live cell). For quantitative viability and proliferation analysis, the cell metabolic activity of the Laponite-containing G10Ly groups (G10L1.0, G10L1.5, G10L2.0) was analyzed and compared to the GelMA alone group (G10L0) at each time point (Fig. 5D). The observed cell viability represents the sum of the mitochondrial activities of all cells (tumor cells, fibroblasts) that make up the 3D microtumor. In our results, the cell viability difference was insignificant in all groups except for the G10L1.5 group. Interestingly, the G10L1.5 group showed a significant increase in cell viability and proliferation compared to the G10L0 group.

Next, we analyzed the cell distribution over time (up to 7 days) in the 3D bioprinted structure of each cell component (tumor cell, fibroblast) constituting the 3D microtumor (Fig. 5E). To this end, we labeled tumor cells and fibroblasts using green and red fluorescence live cell trackers, respectively. Interestingly, the presence of Laponite was observed to influence cellular aggregation. In the GelMA alone group, tumor cells and fibroblasts were relatively evenly distributed throughout the 3D bioprinted structures from Day 1 to Day 7. On the other hand, in the G10Ly group containing Laponite, fibroblast aggregates were observed from Day 1 and increased throughout the experiment period. As the amount of Laponite increased (1.0, 1.5, and 2.0%), the number and size of cellular aggregation islands increased. In particular, tumor cells were mixed with fibroblasts to show overlapping fluorescence signals rather than forming a cell aggregate composed of only cancer cells. The fluorescence overlap (co-localization) and interactions between tumor cells and fibroblasts are prominent in the G10L1.5 group. The G10L2.0 group is observed to constitute larger cellular aggregates composed mainly of fibroblasts encapsulating the cancer cells.

Our results suggest that the amount and presence of Laponite in GelMA/Laponite bioinks may influence the cellular behavior of tumor cells/fibroblasts in the co-culture 3D microtumors. According to previous studies, 2D synthetic silicate nanoparticles such as Laponite can directly attach to the cell surface, be absorbed into the cytoplasm, and interact with cells [67, 68]. In this respect, our results suggest that Laponite, as one of the main components of bioink, may not simply improve mechanical properties but have biologically active properties, which may have influenced the tumor cell/fibroblast interaction. In order to elucidate the bioactive properties of Laponite in more detail, we performed additional gene and protein expression analysis by culturing co-culture 3D bioprinted pancreatic tumors using GelMA/Laponite composite hydrogels of various compositions.

3.6. Gene and protein expression analysis of 3D bioprinting pancreatic tumor-stroma organotypic microtumors

Growth factors such as VEGF, PDGF-β receptor, and IGF1 have been shown to affect cancer cell survival, progression, and chemoresistance in various types of cancer, including pancreatic cancer [69, 70]. In particular, VEGF acts as a mitogen for endothelial cells. Its overexpression in pancreatic cancer is associated with angiogenesis, increased tumor size, and reduced patient survival [69, 71]. As mentioned earlier, PDAC is often characterized by significant fibrosis and dysregulated TGF-β signaling [72, 73]. Additionally, vimentin, a mesenchymal cell marker, has been reported to help diagnose circulating tumor cells in pancreatic cancer [74]. In one clinical study, the proliferating cell nuclear antigen (PCNA) was expressed less than 5% of cases of chronic pancreatitis. At the same time, adenocarcinoma showed significant upregulation (53%) [75].

To what concern genes related to the activation of fibroblast into CAFs, the gene set for CAF signature was composed of *COL1A1*, *COL1A2* [76], *VEGF*, *TGFβ1* [77, 78], *fibronectin* [79, 80], *IGF1* [81–83], and *VIM* [84, 85]. In addition to these genes, CAFs also gain further secretory phenotypes and extracellular matrix production/remodeling [84]. *COL1A1* and *COL1A2* are recognized to compose CAF transcriptional signatures and are associated with EMT signatures in TME [76]. CAFs can also produce many growth factors and proinflammatory cytokines. Notably, *TGFβ1* and *VEGF* promote tumor progression, chronic tumor fibrosis, and angiogenesis [77, 78]. Fibronectin from CAFs mediates CAF-cancer cell association and directional migration [79, 80]. CAFs produce an ECM rich in fibronectin with anisotropic fiber orientation, guiding cancer cells to migrate directionally. *IGF1* secreted by CAFs can stimulate the motility of PDAC cells [81]. In addition, paracrine interaction between CAFs and cancer cells through *IGF1* can promote EMT and induce resistance to chemotherapy [82, 83]. *VIM* expression in CAFs from PDAC patients is associated with significantly shorter overall survival [84]. *VIM* expression in CAFs is related to tumorigenesis, metastasis, recurrence, drug resistance, and poor prognosis in patients with several other cancers [85].

Considering the genetic expression characteristics of pancreatic cancer, the mRNA expression changes in cancer cells and fibroblasts according to the change in the Laponite ratio of GelMA/Laponite composite hydrogels were analyzed through real-time PCR technique. A Laponite-free G10L0 bioink was used as a control. To evaluate the effects of Laponite on tumor cells and fibroblasts, respectively, we designed human primers to analyze the mRNA expression levels of tumor cells in microtumors and designed mouse primers to analyze the fibroblast-related mRNA expression levels. Studies of tumor/fibroblast interactions using cells of different species have been reported, particularly experiments using human tumor cells and mouse fibroblasts [86–88]. Although species-specific primers that detect each mouse and human gene have been designed separately, it is worth noting that gene homology within mammals can influence the level of expression of each phenotype.

As shown in Fig. 6, the change in the ratio of Laponite causes a significant difference in the mRNA expression level of both the tumor-related gene and the fibroblast-related gene. First, the expression levels of growth factors, tissue remodeling, mesenchymal phenotype,

stemness, proliferation, and cell cycle-related genes were evaluated with tumor-related genes in a 3D bioprinted microtumor (Fig 6A). As the overall ratio of Laponite increased, tumor growth factors (*VEGF*) and remodeling-related genes (*SNAI1, TGFb1, MMP2*) were upregulated. In contrast, proliferation and cell cycle-related gene expressions (*Ki67, CDK2, CDK4, CDK6, PCNA*) were down-regulated. It was also observed that the stemness (*OCT4, Nanog*) and mesenchymal phenotype-related genes (*VIM, FBN*) were specifically upregulated when the ratio of Laponite was 1.5% (G10L1.5). In the quantitative analysis of individual genes, *VEGF* expression increased significantly with Laponite ratio (*vs.* G10L1.0; ~10-fold, *vs.* G10L1.5 and G10L2.0; ~20-fold). *PDGFBR1* mRNA expression peaked at 1.5% (G10L1.5) of Laponite and decreased at 2.0% (G10L2.0) (Fig 6B). On the other hand, *VIM* and *PCNA* mRNA expression levels were significantly downregulated in G10L1.0 and G10L2.0 compared to G10L0. Interestingly, G10L1.5 showed comparatively higher *VIM* and *PCNA* mRNA expressions.

As for fibroblast-related genes, in addition to gene expressions related to growth factors, tissue remodeling, ECM molecules, and mesenchymal phenotype, the expression of genes associated with the activation of fibroblasts into CAFs was also evaluated in a 3D bioprinted microtumor composed of G10Ly composite hydrogel (Fig 6C). Interestingly, adding Laponite resulted in an overall upregulation of the diverse gene pools associated with fibroblasts. Especially mRNA expression levels of growth factors (*VEGF, IGF1, FGF2, PDGFα*), tissue remodeling (*TGFβR1, TGFβR2, MMP1a, TIMP1*), and ECM molecule-related genes (*COL1A1, COL1A2, LAMB1, LAMC1, Fibronectin, NES*) were upregulated with an increasing ratio of Laponite (0 to 2.0%) in 3D microtumors. However, interestingly, *VIM*, which is a representative mesenchymal phenotype, and specific ECM-related molecules (*TnC, PCOLCE2, BGN*) showed upregulation peaks at 1.5% of Laponite (G10L1.5) in the 3D microtumor. In quantitative analysis, similar to the expression pattern of tumor-related genes, the amount of *VEGF* expression, known to be highly expressed in CAFs and promote tumor progression, chronic tumor fibrosis, and angiogenesis [77, 78], significantly increased with increasing Laponite ratio (*vs.* G10L1.0 ~30-fold; *vs.* G10L1.5 ~50-fold; *vs.* G10L2.0 ~60-fold) (Fig 6D). *TGFβ1*, expressed in CAFs, which is involved in tissue remodeling and fibrosis, and *IGF1*, which stimulates the motility of PDAC cells [81] and promotes EMT, and induces resistance to chemotherapy [82, 83], also showed remarkable upregulation at 1.5% or more of Laponite (*TGFβ1* >40-fold; *IGF1* >10-fold). Interestingly, the G10L1.5 group showed higher *VIM* expression than other G10Ly groups, similar to the tumor-associated gene expression pattern observed in Fig. 6B.

Finally, immunoblot analysis was performed to evaluate the biological changes of protein levels according to the % change of Laponite in 3D microtumors composed of GelMA and Laponite hydrogel (Fig. 6E). As the percentage of Laponite in the microtumor structure increased, the expression levels of VEGF and IGF1 proteins increased compared to the GelMA-only group. In contrast, in the GelMA-only group, the expression levels of VIM and TGFβ1 proteins were not down-regulated, as was observed in the gene results. The group with 1% Laponite (G10L1.0) showed significantly lower VIM and TGFβ1 protein expression levels. In contrast, the 1.5% (G10L1.5) and 2.0% (G10L2.0) Laponite groups showed similar levels of VIM expression to the GelMA-only group. Gene and protein expression results suggest that when fabricating a 3D microtumor construct using GelMA-

based bioink, adding Laponite can exhibit biological effects on cancer and fibroblasts. In addition, the increased expression of genes related to CAFs suggests the possibility of utilizing GelMA/Laponite composite hydrogels for modeling and studying the activation of fibroblasts into CAFs in PDAC. Although GelMA/Laponite composite hydrogels evaluated in this study showed promising results in studying PDAC organoids generated from the co-culture of tumor cells and fibroblasts and the activation of fibroblasts into CAFs in *in vitro* environments, *in vivo* studies are necessary to verify the engraftment and the ability of this model to mimic the PDAC heterogeneity.

GelMA-based hydrogels are excellent choices for modeling and studying PDAC. Increasing stiffness is known to alter cellular behavior and trigger internal signaling pathways. Furthermore, desmoplastic tumors are associated with a poor prognosis, including PDAC. Due to its porous, adjustable mechanical properties and excellent *in vitro* and *in vivo* biocompatibility, GelMA-based hydrogels have been extensively explored to model desmoplastic tumors such as PDAC.

In a recent work by our group, hybrid methacrylate hyaluronic acid/GelMA (HAMA/GelMA) hydrogels were evaluated regarding their ability to model desmoplastic PDAC [89]. In the study, spheroids composed of co-culture of PDAC cells and fibroblasts were cultured within HAMA/GelMA hydrogels mimicking different levels of tissue stiffness, from healthy pancreas tissue to hyper desmoplastic PDAC. The stiffness of the hydrogels was adjusted by varying crosslinking time for HAMA/GelMA hydrogels composed of 1% HAMA and 10% GelMA. The results showed that higher expression levels of markers associated with proliferation, EMT, mechanotransduction, and progression are observed for cancer-fibroblast spheroids cultured in hyper desmoplastic matrix-mimicking hydrogels. In contrast, the same trend was only observed when spheroids were cultured in desmoplastic matrix-mimicking hydrogels with *TGFβ1* supplementation.

In another study by Zhang et al., GelMA hydrogels prepared with varying methacrylation degrees and prepolymer concentrations were utilized to tune hydrogels' porosity and stiffness [90]. These hydrogels with tunable properties were used to study stiffness-dependent PDAC progression and tumor immunosuppression. Their assessments in *in vitro* and *in vivo* models suggested the GelMA hydrogel with high stiffness affects cell morphology, cytoskeleton remodeling, and malignant biological behaviors in PDAC.

Laponite has been known to have osteogenic bioactive properties in human MSCs or preosteoblasts [30, 31, 91]. Among these studies, whole transcriptome-level RNA-sequencing analysis of human MSCs treated with Laponite showed that Laponite could regulate thousands of human genes [91]. The authors note that Laponite has implicated several biological processes, including protein targeting to membranes, responses to growth factors, morphogenesis of cell differentiation, positive regulation of mitogen-activated protein kinase (MAPK) cascade, cWnt signaling pathway, and TGFβ receptor signaling. Considering these previous studies with our results, we can suggest that Laponite has bioactive properties that can enhance fibrotic/ECM-related gene expression in a pancreatic cancer model characterized by fibroblast aggregation and CAF-cancer cell association. In our results, we confirmed that Laponite could influence the genes involved in growth factor,

mesenchymal cell phenotype, ECM formation, and CAFs phenotypes among the genes of fibroblasts. These results may explain the effect of Laponite on its bioactive properties on tumor cells/fibroblasts, which has been questioned in cell distribution studies in 3D microtumors (Fig 5E). That is, as the concentration of Laponite increases, aggregation of fibroblasts and CAF-cancer cell association in 3D bioprinted microtumors may be prominent due to the upregulation of *TGFβ*, *IGF1*, and *MMP*, and *ECM-related genes* caused by Laponite. In addition, although both epithelial and mesenchymal cells can be affected up to G10L1.5, which is not saturated with an electrostatic charge, the pattern of inducing the mesenchymal phenotype can become more pronounced when the Laponite content is further increased.

4. Conclusion

In this study, we developed a nanoengineered ion-covalent cross-linkable bioink to construct 3D bioprinted organotypic tumor models. In particular, Laponite, which has been used to compose shear-thinning materials in tissue engineering, was introduced into GelMA to produce a nanoengineered ionic-covalently cross-linkable bioink that exhibits a unique ionic charge to improve retention of biological factors released by the encapsulated cells and assist in paracrine signals. In our results, composite hydrogels with low Laponite:GelMA ratios (G10L1.0, G10L1.5, and G10L2.0) exhibited high biocompatibility and improved rheological and mechanical properties for 3D bioprinting. In particular, GelMA/Laponite hydrogel efficiently promotes the proliferation of MIA PaCa-2 cells and fibroblasts, providing an excellent microenvironment that promotes Laponite concentration-dependent cell migration for self-assembly into cancer matrix aggregates. Furthermore, changes in the Laponite ratio have been shown to cause significant changes in mRNA expression levels of both tumor-associated and fibroblast-associated genes. GelMA/Laponite composite bioink caused tissue remodeling of cancer cells and upregulation of genes that could promote desmoplastic fibroblast phenotype and ECM accumulation in the 3D bioprinted microtumor. Taken together, GelMA/Laponite composite hydrogel has mechanical properties suitable for 3D bioprinting and improves tumor cell/mesenchymal stromal cell interaction for cell survival, proliferation, and cancer-stromal aggregation. These GelMA/Laponite bioink compositions are not limited to the pancreatic cancer cell lines we studied here. However, further biological underlying mechanism evaluation studies based on more detailed cancer biology may be required depending on the source of the forming tumor cell line. These studies are expected to serve as a basis for 3D cancer modeling potential of Laponite-based hydrogels.

Supplementary Material

Refer to Web version on PubMed Central for supplementary material.

Acknowledgements

The authors acknowledge U.S. fundings from the National Institutes of Health (HL140951, HL137193, CA257558, DK130566), National Aeronautics and Space Administration (80NSSC19M0200, 80NSSC22M0132), Department of Defense (MCS1292-20-01), and National Science Foundation (1712391). This work is also supported by the College of Science and Mathematics at California State University Northridge (CSUN); Sidney Stern Memorial Trust (to J.A.K.); Sutter family (to J.A.K); Aylozyan Family Foundation (to J.A.K.); and NIH NIGMS grant

SC1GM121182 (to J.A.K.). The cell lines (MIA PaCa-2 and C3H10T1/2, Clone 8) utilized in this research were provided by Dr. Jonathan Kelber from the Developmental Oncogene Laboratory at CSUN.

Data availability statement

All data that support the findings of this study are included within the article (and any supplementary files).

References

[1]. Jin M-Z, Jin W-L, The updated landscape of tumor microenvironment and drug repurposing, Signal Transduction and Targeted Therapy 5(1) (2020) 166. [PubMed: 32843638]

[2]. Tomás-Bort E, Kieler M, Sharma S, Candido JB, Loessner D, 3D approaches to model the tumor microenvironment of pancreatic cancer, Theranostics 10(11) (2020) 5074–5089. [PubMed: 32308769]

[3]. Binnewies M, Roberts EW, Kersten K, Chan V, Fearon DF, Merad M, Coussens LM, Gabrilovich DI, Ostrand-Rosenberg S, Hedrick CC, Vonderheide RH, Pittet MJ, Jain RK, Zou W, Howcroft TK, Woodhouse EC, Weinberg RA, Krummel MF, Understanding the tumor immune microenvironment (TIME) for effective therapy, Nature Medicine 24(5) (2018) 541–550.

[4]. Ho WJ, Jaffee EM, Zheng L, The tumour microenvironment in pancreatic cancer — clinical challenges and opportunities, Nature Reviews Clinical Oncology 17(9) (2020) 527–540.

[5]. Jensen C, Teng Y, Is It Time to Start Transitioning From 2D to 3D Cell Culture?, Frontiers in Molecular Biosciences 7(33) (2020).

[6]. Murphy SV, Atala A, 3D bioprinting of tissues and organs, Nature Biotechnology 32(8) (2014) 773–785.

[7]. Horejs C, Organ chips, organoids and the animal testing conundrum, Nature Reviews Materials 6(5) (2021) 372–373. [PubMed: 33936776]

[8]. Rodrigues J, Heinrich MA, Teixeira LM, Prakash J, 3D In Vitro Model (R)evolution: Unveiling Tumor-Stroma Interactions, Trends in Cancer 7(3) (2021) 249–264. [PubMed: 33218948]

[9]. Ferreira LP, Gaspar VM, Mano JF, Design of spherically structured 3D in vitro tumor models -Advances and prospects, Acta Biomaterialia 75 (2018) 11–34. [PubMed: 29803007]

[10]. Kirsch M, Birnstein L, Pepelanova I, Handke W, Rach J, Seltsam A, Scheper T, Lavrentieva A, Gelatin-Methacryloyl (GelMA) Formulated with Human Platelet Lysate Supports Mesenchymal Stem Cell Proliferation and Differentiation and Enhances the Hydrogel's Mechanical Properties, Bioengineering 6(3) (2019) 76. [PubMed: 31466260]

[11]. Ding R, Wei X, Liu Y, Wang Y, Xing Z, Wang L, Liu H, Fan Y, Epidermal growth factor-loaded microspheres/hydrogel composite for instant hemostasis and liver regeneration, Smart Materials in Medicine 4 (2023) 173–182.

[12]. Augustine R, Hasan A, Dalvi YB, Rehman SRU, Varghese R, Unni RN, Yalcin HC, Alfkey R, Thomas S, Al Moustafa A-E, Growth factor loaded in situ photocrosslinkable poly(3-hydroxybutyrate-co-3-hydroxyvalerate)/gelatin methacryloyl hybrid patch for diabetic wound healing, Materials Science and Engineering: C 118 (2021) 111519. [PubMed: 33255074]

[13]. Modaresifar K, Hadjizadeh A, Niknejad H, Design and fabrication of GelMA/chitosan nanoparticles composite hydrogel for angiogenic growth factor delivery, Artificial Cells, Nanomedicine, and Biotechnology 46(8) (2018) 1799–1808.

[14]. Recent Advances on Bioprinted Gelatin Methacrylate-Based Hydrogels for Tissue Repair, Tissue Engineering Part A 27(11-12) (2021) 679–702. [PubMed: 33499750]

[15]. Janmaleki M, Liu J, Kamkar M, Azarmanesh M, Sundararaj U, Nezhad AS, Role of temperature on bio-printability of gelatin methacryloyl bioink in two-step cross-linking strategy for tissue engineering applications, Biomedical Materials 16(1) (2020) 015021. [PubMed: 33325382]

[16]. Gaharwar AK, Cross LM, Peak CW, Gold K, Carrow JK, Brokesh A, Singh KA, 2D Nanoclay for Biomedical Applications: Regenerative Medicine, Therapeutic Delivery, and Additive Manufacturing, Advanced Materials 31(23) (2019) 1900332.

[17]. Maisanaba S, Pichardo S, Puerto M, Gutiérrez-Praena D, Cameán AM, Jos A, Toxicological evaluation of clay minerals and derived nanocomposites: A review, Environmental Research 138 (2015) 233–254. [PubMed: 25732897]

[18]. Tan Y, Xu S, Wu R, Du J, Sang J, Wang J, A gradient Laponite-crosslinked nanocomposite hydrogel with anisotropic stress and thermo-response, Applied Clay Science 148 (2017) 77–82.

[19]. Ruzicka B, Zaccarelli E, A fresh look at the Laponite phase diagram, Soft Matter 7(4) (2011) 1268–1286.

[20]. Sheikhi A, Afewerki S, Oklu R, Gaharwar AK, Khademhosseini A, Effect of ionic strength on shear-thinning nanoclay–polymer composite hydrogels, Biomaterials Science 6(8) (2018) 2073–2083. [PubMed: 29944151]

[21]. Ahlfeld T, Cidonio G, Kilian D, Duin S, Akkineni AR, Dawson JI, Yang S, Lode A, Oreffo ROC, Gelinsky M, Development of a clay based bioink for 3D cell printing for skeletal application, Biofabrication 9(3) (2017) 034103. [PubMed: 28691691]

[22]. Gaharwar AK, Mihaila SM, Swami A, Patel A, Sant S, Reis RL, Marques AP, Gomes ME, Khademhosseini A, Bioactive Silicate Nanoplatelets for Osteogenic Differentiation of Human Mesenchymal Stem Cells, Advanced Materials 25(24) (2013) 3329–3336. [PubMed: 23670944]

[23]. Xue C, Xie H, Eichenbaum J, Chen Y, Wang Y, van den Dolder FW, Lee J, Lee K, Zhang S, Sun W, Sheikhi A, Ahadian S, Ashammakhi N, Dokmeci MR, Kim H-J, Khademhosseini A, Synthesis of Injectable Shear-Thinning Biomaterials of Various Compositions of Gelatin and Synthetic Silicate Nanoplatelet, Biotechnology Journal 15(8) (2020) 1900456.

[24]. Kiaee G, Dimitrakakis N, Sharifzadeh S, Kim HJ, Avery RK, Moghaddam KM, Haghiniaz R, Yalcintas EP, Barros N, Karamikamkar S, Laponite-based Nanomaterials For Drug Delivery, Advanced Healthcare Materials (2022) 2102054.

[25]. Gaharwar AK, Avery RK, Assmann A, Paul A, McKinley GH, Khademhosseini A, Olsen BD, Shear-Thinning Nanocomposite Hydrogels for the Treatment of Hemorrhage, ACS Nano 8(10) (2014) 9833–9842. [PubMed: 25221894]

[26]. Avery RK, Albadawi H, Akbari M, Zhang YS, Duggan MJ, Sahani DV, Olsen BD, Khademhosseini A, Oklu R, An injectable shear-thinning biomaterial for endovascular embolization, Science translational medicine 8(365) (2016) 365ra156–365ra156.

[27]. Albadawi H, Altun I, Hu J, Zhang Z, Panda A, Kim HJ, Khademhosseini A, Oklu R, Nanocomposite Hydrogel with Tantalum Microparticles for Rapid Endovascular Hemostasis, Advanced Science 8(1) (2021) 2003327.

[28]. Lee J, Wang Y, Xue C, Chen Y, Qu M, Thakor J, Zhou X, Barros NR, Falcone N, Young P, van den Dolder FW, Lee K, Zhu Y, Cho H-J, Sun W, Zhao B, Ahadian S, Jucaud V, Dokmeci MR, Khademhosseini A, Kim H-J, pH-Responsive doxorubicin delivery using shear-thinning biomaterials for localized melanoma treatment, Nanoscale 14(2) (2022) 350–360. [PubMed: 34908077]

[29]. Becher TB, Mendonça MCP, de Farias MA, Portugal RV, de Jesus MB, Ornelas C, Soft Nanohydrogels Based on Laponite Nanodiscs: A Versatile Drug Delivery Platform for Theranostics and Drug Cocktails, ACS Applied Materials & Interfaces 10(26) (2018) 21891–21900. [PubMed: 29889487]

[30]. Liu B, Li J, Lei X, Miao S, Zhang S, Cheng P, Song Y, Wu H, Gao Y, Bi L, Pei G, Cell-loaded injectable gelatin/alginate/LAPONITE® nanocomposite hydrogel promotes bone healing in a critical-size rat calvarial defect model, RSC Advances 10(43) (2020) 25652–25661. [PubMed: 35518607]

[31]. Zhai X, Ruan C, Ma Y, Cheng D, Wu M, Liu W, Zhao X, Pan H, Lu WW, 3D-Bioprinted Osteoblast-Laden Nanocomposite Hydrogel Constructs with Induced Microenvironments Promote Cell Viability, Differentiation, and Osteogenesis both In Vitro and In Vivo, Advanced Science 5(3) (2018) 1700550. [PubMed: 29593958]

[32]. Quint JP, Samandari M, Abbasi L, Mollocana E, Rinoldi C, Mostafavi A, Tamayol A, Nanoengineered myogenic scaffolds for skeletal muscle tissue engineering, Nanoscale 14(3) (2022) 797–814. [PubMed: 34951427]

[33]. Carrow JK, Cross LM, Reese RW, Jaiswal MK, Gregory CA, Kaunas R, Singh I, Gaharwar AK, Widespread changes in transcriptome profile of human mesenchymal stem cells induced

by two-dimensional nanosilicates, Proc Natl Acad Sci U S A 115(17) (2018) E3905–E3913. [PubMed: 29643075]

[34]. Suklabaidya S, Dash P, Das B, Suresh V, Sasmal PK, Senapati S, Experimental models of pancreatic cancer desmoplasia, Laboratory Investigation 98(1) (2018) 27–40. [PubMed: 29155423]

[35]. Öhlund D, Handly-Santana A, Biffi G, Elyada E, Almeida AS, Ponz-Sarvise M, Corbo V, Oni TE, Hearn SA, Lee EJ, Chio IIC, Hwang C-I, Tiriac H, Baker LA, Engle DD, Feig C, Kultti A, Egeblad M, Fearon DT, Crawford JM, Clevers H, Park Y, Tuveson DA, Distinct populations of inflammatory fibroblasts and myofibroblasts in pancreatic cancer, Journal of Experimental Medicine 214(3) (2017) 579–596. [PubMed: 28232471]

[36]. Tang Q-Q, Otto TC, Lane MD, Commitment of C3H10T1/2 pluripotent stem cells to the adipocyte lineage, Proceedings of the National Academy of Sciences 101(26) (2004) 9607–9611.

[37]. Wang M, Su Y, Sun H, Wang T, Yan G, Ran X, Wang F, Cheng T, Zou Z, Induced endothelial differentiation of cells from a murine embryonic mesenchymal cell line C3H/10T1/2 by angiogenic factors in vitro, Differentiation 79(1) (2010) 21–30. [PubMed: 19726123]

[38]. Cheng LC, Zhang X, Abhinav K, Nguyen JA, Baboo S, Martinez-Bartolomé S, Branon TC, Ting AY, Loose E, Yates JR 3rd, Gerace L, Shared and Distinctive Neighborhoods of Emerin and Lamin B Receptor Revealed by Proximity Labeling and Quantitative Proteomics, J Proteome Res 21(9) (2022) 2197–2210. [PubMed: 35972904]

[39]. Yue K, Trujillo-de Santiago G, Alvarez MM, Tamayol A, Annabi N, Khademhosseini A, Synthesis, properties, and biomedical applications of gelatin methacryloyl (GelMA) hydrogels, Biomaterials 73 (2015) 254–271. [PubMed: 26414409]

[40]. Barros NR, Kim H-J, Gouidie MJ, Lee K, Bandaru P, Banton EA, Sarikhani E, Sun W, Zhang S, Cho H-J, Hartel MC, Ostrovidov S, Ahadian S, Hussain SM, Ashammakhi N, Dokmeci MR, Herculano RD, Lee J, Khademhosseini A, Biofabrication of endothelial cell, dermal fibroblast, and multilayered keratinocyte layers for skin tissue engineering, Biofabrication 13(3) (2021) 035030.

[41]. Wang L, Xu M.-e., Luo L, Zhou Y, Si P, Iterative feedback bio-printing-derived cell-laden hydrogel scaffolds with optimal geometrical fidelity and cellular controllability, Scientific Reports 8(1) (2018) 2802. [PubMed: 29434327]

[42]. Hu JB, Tomov ML, Buikema JW, Chen C, Mahmoudi M, Wu SM, Serpooshan V, Cardiovascular tissue bioprinting: Physical and chemical processes, Applied Physics Reviews 5(4) (2018) 041106. [PubMed: 32550960]

[43]. Ning L, Mehta R, Cao C, Theus A, Tomov M, Zhu N, Weeks ER, Bauser-Heaton H, Serpooshan V, Embedded 3D Bioprinting of Gelatin Methacryloyl-Based Constructs with Highly Tunable Structural Fidelity, ACS Applied Materials & Interfaces 12(40) (2020) 44563–44577. [PubMed: 32966746]

[44]. Ruzicka B, Zaccarelli E, Zulian L, Angelini R, Sztucki M, Moussaïd A, Narayanan T, Sciortino F, Observation of empty liquids and equilibrium gels in a colloidal clay, Nature Materials 10(1) (2011) 56–60. [PubMed: 21151164]

[45]. Schmidt G, Nakatani AI, Butler PD, Han CC, Small-Angle Neutron Scattering from Viscoelastic Polymer–Clay Solutions, Macromolecules 35(12) (2002) 4725–4732.

[46]. Cedervall T, Lynch I, Lindman S, Berggård T, Thulin E, Nilsson H, Dawson KA, Linse S, Understanding the nanoparticle–protein corona using methods to quantify exchange rates and affinities of proteins for nanoparticles, Proceedings of the National Academy of Sciences 104(7) (2007) 2050–2055.

[47]. Nel AE, Mädler L, Velegol D, Xia T, Hoek EMV, Somasundaran P, Klaessig F, Castranova V, Thompson M, Understanding biophysicochemical interactions at the nano–bio interface, Nature Materials 8(7) (2009) 543–557. [PubMed: 19525947]

[48]. Schwab A, Levato R, D'Este M, Piluso S, Eglin D, Malda J, Printability and Shape Fidelity of Bioinks in 3D Bioprinting, Chemical Reviews 120(19) (2020) 11028–11055. [PubMed: 32856892]

[49]. Wilson SA, Cross LM, Peak CW, Gaharwar AK, Shear-Thinning and Thermo-Reversible Nanoengineered Inks for 3D Bioprinting, ACS Applied Materials & Interfaces 9(50) (2017) 43449–43458. [PubMed: 29214803]

[50]. Peak CW, Stein J, Gold KA, Gaharwar AK, Nanoengineered Colloidal Inks for 3D Bioprinting, Langmuir 34(3) (2018) 917–925. [PubMed: 28981287]

[51]. Chimene D, Peak CW, Gentry JL, Carrow JK, Cross LM, Mondragon E, Cardoso GB, Kaunas R, Gaharwar AK, Nanoengineered Ionic–Covalent Entanglement (NICE) Bioinks for 3D Bioprinting, ACS Applied Materials & Interfaces 10(12) (2018) 9957–9968. [PubMed: 29461795]

[52]. Mourchid A, Delville A, Lambard J, LeColier E, Levitz P, Phase Diagram of Colloidal Dispersions of Anisotropic Charged Particles: Equilibrium Properties, Structure, and Rheology of Laponite Suspensions, Langmuir 11(6) (1995) 1942–1950.

[53]. Thompson DW, Butterworth JT, The nature of laponite and its aqueous dispersions, Journal of Colloid and Interface Science 151(1) (1992) 236–243.

[54]. Ruzicka B, Zulian L, Ruocco G, Ageing dynamics in Laponite dispersions at various salt concentrations, Philosophical Magazine 87(3-5) (2007) 449–458.

[55]. Mongondry P, Tassin JF, Nicolai T, Revised state diagram of Laponite dispersions, Journal of Colloid and Interface Science 283(2) (2005) 397–405. [PubMed: 15721911]

[56]. Lokhande G, Carrow JK, Thakur T, Xavier JR, Parani M, Bayless KJ, Gaharwar AK, Nanoengineered injectable hydrogels for wound healing application, Acta biomaterialia 70 (2018) 35–47. [PubMed: 29425720]

[57]. Boyer C, Figueiredo L, Pace R, Lesoeur J, Rouillon T, Visage CL, Tassin J-F, Weiss P, Guicheux J, Rethore G, Laponite nanoparticle-associated silated hydroxypropylmethyl cellulose as an injectable reinforced interpenetrating network hydrogel for cartilage tissue engineering, Acta Biomaterialia 65 (2018) 112–122. [PubMed: 29128532]

[58]. Thakur A, Jaiswal MK, Peak CW, Carrow JK, Gentry J, Dolatshahi-Pirouz A, Gaharwar AK, Injectable shear-thinning nanoengineered hydrogels for stem cell delivery, Nanoscale 8(24) (2016) 12362–12372. [PubMed: 27270567]

[59]. Heid S, Boccaccini AR, Advancing bioinks for 3D bioprinting using reactive fillers: A review, Acta Biomaterialia 113 (2020) 1–22. [PubMed: 32622053]

[60]. Purwada A, Jaiswal MK, Ahn H, Nojima T, Kitamura D, Gaharwar AK, Cerchietti L, Singh A, Ex vivo engineered immune organoids for controlled germinal center reactions, Biomaterials 63 (2015) 24–34. [PubMed: 26072995]

[61]. Schnittert J, Bansal R, Prakash J, Targeting Pancreatic Stellate Cells in Cancer, Trends in Cancer 5(2) (2019) 128–142. [PubMed: 30755305]

[62]. Baghban R, Roshangar L, Jahanban-Esfahlan R, Seidi K, Ebrahimi-Kalan A, Jaymand M, Kolahian S, Javaheri T, Zare P, Tumor microenvironment complexity and therapeutic implications at a glance, Cell Communication and Signaling 18(1) (2020) 1–19. [PubMed: 31900175]

[63]. Quail DF, Joyce JA, Microenvironmental regulation of tumor progression and metastasis, Nature medicine 19(11) (2013) 1423–1437.

[64]. Czekay RP, Cheon DJ, Samarakoon R, Kutz SM, Higgins PJ, Cancer-Associated Fibroblasts: Mechanisms of Tumor Progression and Novel Therapeutic Targets, Cancers (Basel) 14(5) (2022).

[65]. Kuen J, Darowski D, Kluge T, Majety M, Pancreatic cancer cell/fibroblast co-culture induces M2 like macrophages that influence therapeutic response in a 3D model, PloS one 12(7) (2017) e0182039. [PubMed: 28750018]

[66]. Shan T, Chen S, Chen X, Lin WR, Li W, Ma J, Wu T, Cui X, Ji H, Li Y, Cancer-associated fibroblasts enhance pancreatic cancer cell invasion by remodeling the metabolic conversion mechanism, Oncology reports 37(4) (2017) 1971–1979. [PubMed: 28260082]

[67]. Mihaila SM, Gaharwar AK, Reis RL, Khademhosseini A, Marques AP, Gomes ME, The osteogenic differentiation of SSEA-4 sub-population of human adipose derived stem cells using silicate nanoplatelets, Biomaterials 35(33) (2014) 9087–9099. [PubMed: 25123923]

[68]. Castro-Smirnov FA, Ayache J, Bertrand J-R, Dardillac E, Le Cam E, Piétrement O, Aranda P, Ruiz-Hitzky E, Lopez BS, Cellular uptake pathways of sepiolite nanofibers and DNA transfection improvement, Scientific reports 7(1) (2017) 1–10. [PubMed: 28127051]

[69]. Xelwa N, Candy GP, Devar J, Omoshoro-Jones J, Smith M, Nweke EE, Targeting Growth Factor Signaling Pathways in Pancreatic Cancer: Towards Inhibiting Chemoresistance, Frontiers in oncology 11 (2021) 683788. [PubMed: 34195085]

[70]. Juhász M, Nitsche B, Malfertheiner P, Ebert MP, Implications of growth factor alterations in the treatment of pancreatic cancer, Molecular Cancer 2 (2003) 1–7. [PubMed: 12537587]

[71]. Lim YJ, Lee JK, Park CK, Song SY, Jang WY, Ha HY, Park DI, Lee KT, Paik SW, Yoo BC, Prognostic value of VEGF in human pancreatic ductal adenocarcinoma, The Korean Journal of Internal Medicine 19(1) (2004) 10. [PubMed: 15053037]

[72]. Hilbig A, Oettle H, Transforming growth factor beta in pancreatic cancer, Current pharmaceutical biotechnology 12(12) (2011) 2158–2164. [PubMed: 21619533]

[73]. Porcelli L, Iacobazzi RM, Di Fonte R, Serratì S, Intini A, Solimando AG, Brunetti O, Calabrese A, Leonetti F, Azzariti A, CAFs and TGF-β signaling activation by mast cells contribute to resistance to gemcitabine/nabpaclitaxel in pancreatic cancer, Cancers 11(3) (2019) 330. [PubMed: 30866547]

[74]. Wei T, Zhang X, Zhang Q, Yang J, Chen Q, Wang J, Li X, Chen J, Ma T, Li G, Vimentin-positive circulating tumor cells as a biomarker for diagnosis and treatment monitoring in patients with pancreatic cancer, Cancer Letters 452 (2019) 237–243. [PubMed: 30905814]

[75]. Lee C, Georgiou T, Rode J, Proliferating cell nuclear antigen (PCNA) in pancreatic adenocarcinoma, Pathology-Research and Practice 189(5) (1993) 527–529. [PubMed: 8104328]

[76]. Szabo PM, Vajdi A, Kumar N, Tolstorukov MY, Chen BJ, Edwards R, Ligon KL, Chasalow SD, Chow K-H, Shetty A, Bolisetty M, Holloway JL, Golhar R, Kidd BA, Hull PA, Houser J, Vlach L, Siemers NO, Saha S, Cancer-associated fibroblasts are the main contributors to epithelial-to-mesenchymal signatures in the tumor microenvironment, Scientific Reports 13(1) (2023) 3051. [PubMed: 36810872]

[77]. Shi X, Young CD, Zhou H, Wang X, Transforming Growth Factor-β Signaling in Fibrotic Diseases and Cancer-Associated Fibroblasts, Biomolecules 10(12) (2020).

[78]. Liu T, Han C, Wang S, Fang P, Ma Z, Xu L, Yin R, Cancer-associated fibroblasts: an emerging target of anti-cancer immunotherapy, Journal of Hematology & Oncology 12(1) (2019) 86. [PubMed: 31462327]

[79]. Erdogan B, Ao M, White LM, Means AL, Brewer BM, Yang L, Washington MK, Shi C, Franco OE, Weaver AM, Hayward SW, Li D, Webb DJ, Cancer-associated fibroblasts promote directional cancer cell migration by aligning fibronectin, J Cell Biol 216(11) (2017) 3799–3816. [PubMed: 29021221]

[80]. Zhang J, Chen M, Fang C, Luo P, A cancer-associated fibroblast gene signature predicts prognosis and therapy response in patients with pancreatic cancer, Front Oncol 12 (2022) 1052132. [PubMed: 36465388]

[81]. Hirakawa T, Yashiro M, Doi Y, Kinoshita H, Morisaki T, Fukuoka T, Hasegawa T, Kimura K, Amano R, Hirakawa K, Pancreatic Fibroblasts Stimulate the Motility of Pancreatic Cancer Cells through IGF1/IGF1R Signaling under Hypoxia, PLOS ONE 11(8) (2016) e0159912. [PubMed: 27487118]

[82]. Long X, Xiong W, Zeng X, Qi L, Cai Y, Mo M, Jiang H, Zhu B, Chen Z, Li Y, Cancer-associated fibroblasts promote cisplatin resistance in bladder cancer cells by increasing IGF-1/ERβ/Bcl-2 signalling, Cell Death & Disease 10(5) (2019) 375. [PubMed: 31076571]

[83]. Yi Y, Zeng S, Wang Z, Wu M, Ma Y, Ye X, Zhang B, Liu H, Cancer-associated fibroblasts promote epithelial-mesenchymal transition and EGFR-TKI resistance of non-small cell lung cancers via HGF/IGF-1/ANXA2 signaling, Biochimica et Biophysica Acta (BBA) - Molecular Basis of Disease 1864(3) (2018) 793–803. [PubMed: 29253515]

[84]. Nomura S, Identification, Friend or Foe: Vimentin and α-Smooth Muscle Actin in Cancer-Associated Fibroblasts, Annals of Surgical Oncology 26(13) (2019) 4191–4192. [PubMed: 31605319]

[85]. Zhao Z, Li T, Yuan Y, Zhu Y, What is new in cancer-associated fibroblast biomarkers?, Cell Communication and Signaling 21(1) (2023) 96. [PubMed: 37143134]

[86]. Konitsiotis AD, Chang S-C, Jovanović B, Ciepla P, Masumoto N, Palmer CP, Tate EW, Couchman JR, Magee AI, Attenuation of hedgehog acyltransferase-catalyzed sonic Hedgehog palmitoylation causes reduced signaling, proliferation and invasiveness of human carcinoma cells, PloS one 9(3) (2014) e89899. [PubMed: 24608521]

[87]. Petrova E, Matevossian A, Resh M, Hedgehog acyltransferase as a target in pancreatic ductal adenocarcinoma, Oncogene 34(2) (2015) 263–268. [PubMed: 24469057]

[88]. Damhofer H, Medema JP, Veenstra VL, Badea L, Popescu I, Roelink H, Bijlsma MF, Assessment of the stromal contribution to Sonic Hedgehog-dependent pancreatic adenocarcinoma, Molecular oncology 7(6) (2013) 1031–1042. [PubMed: 23998958]

[89]. Ermis M, Falcone N, Roberto de Barros N, Mecwan M, Haghniaz R, Choroomi A, Monirizad M, Lee Y, Song J, Cho H-J, Zhu Y, Kang H, Dokmeci MR, Khademhosseini A, Lee J, Kim H-J, Tunable hybrid hydrogels with multicellular spheroids for modeling desmoplastic pancreatic cancer, Bioactive Materials 25 (2023) 360–373. [PubMed: 36879666]

[90]. Zhang H, Chen J, Hu X, Bai J, Yin T, Adjustable extracellular matrix rigidity tumor model for studying stiffness dependent pancreatic ductal adenocarcinomas progression and tumor immunosuppression, Bioeng Transl Med 8(3) (2023) e10518. [PubMed: 37206224]

[91]. Carrow JK, Cross LM, Reese RW, Jaiswal MK, Gregory CA, Kaunas R, Singh I, Gaharwar AK, Widespread changes in transcriptome profile of human mesenchymal stem cells induced by two-dimensional nanosilicates, Proceedings of the National Academy of Sciences 115(17) (2018) E3905–E3913.

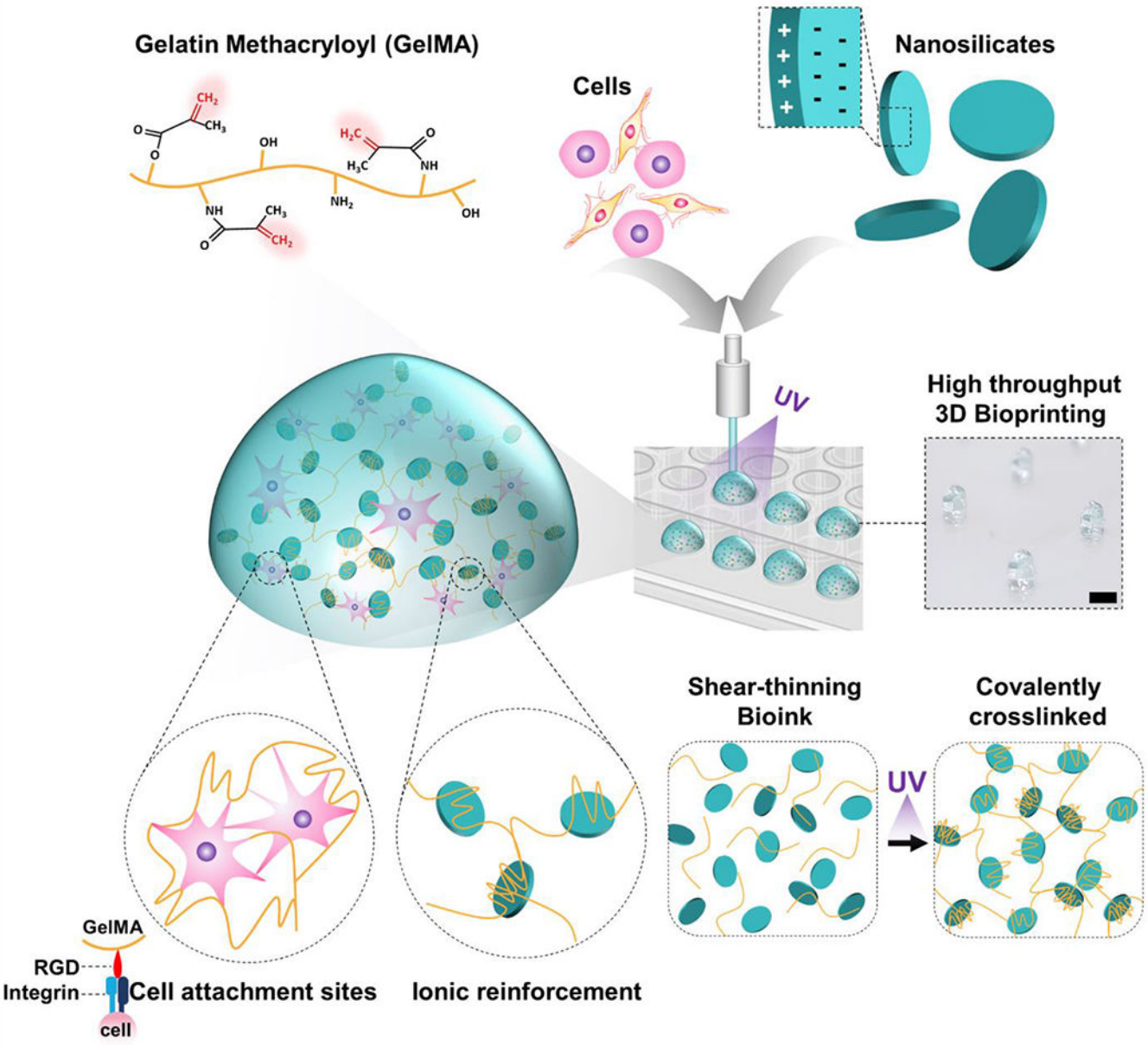

Figure 1. Schematic illustration of the fabrication of nanoengineered composite bioink.

GelMA/Laponite hydrogels combine physical and covalent photo-crosslinking from GelMA and ionic reinforcement from Laponite. It creates a shear-thinning bioink that is highly printable, cell-friendly, and stable after covalent photo-crosslinking. Laponite provides ionic interactions to create a reinforced network, allowing GelMA to behave as a shear-thinning bioink with self-healing properties. In addition, after photo-crosslinking of the GelMA component, Laponite reinforcement synergistically enhances mechanical strength. Scale bar: 2 mm.

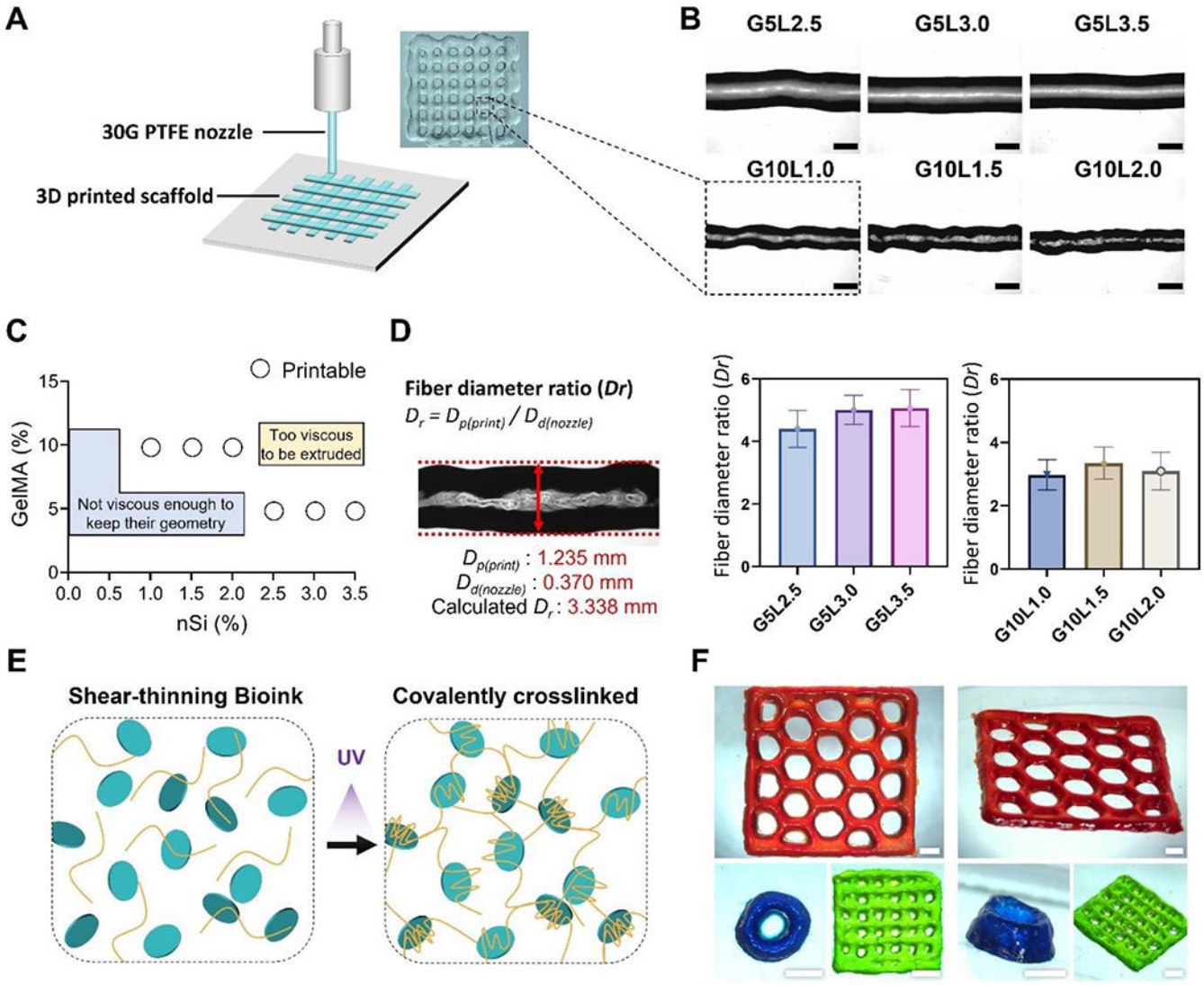

Figure 2. Printability characterization of the GelMA/Laponite composite hydrogels.

A) Schematic representation of 3D printing process and a digital image of a 3D printed grid structure. B) bright-field microscopy (BF) images of printed fibers from different GelMA/Laponite composite hydrogels (Scale bar: 1 mm). C) Representation of printable and non-printable compositions. D) Fiber diameter ratio (D_r) of GelMA/Laponite composite hydrogels extruded through a 30G PTFE nozzle. Data are means ± SD (n = 10). E) Schematic representation of the shear-thinning GelMA/Laponite composite hydrogel before and after photo-crosslinking. F) Representative digital images of 3D printed multiple layers with different geometries (Scale bar: 2 mm).

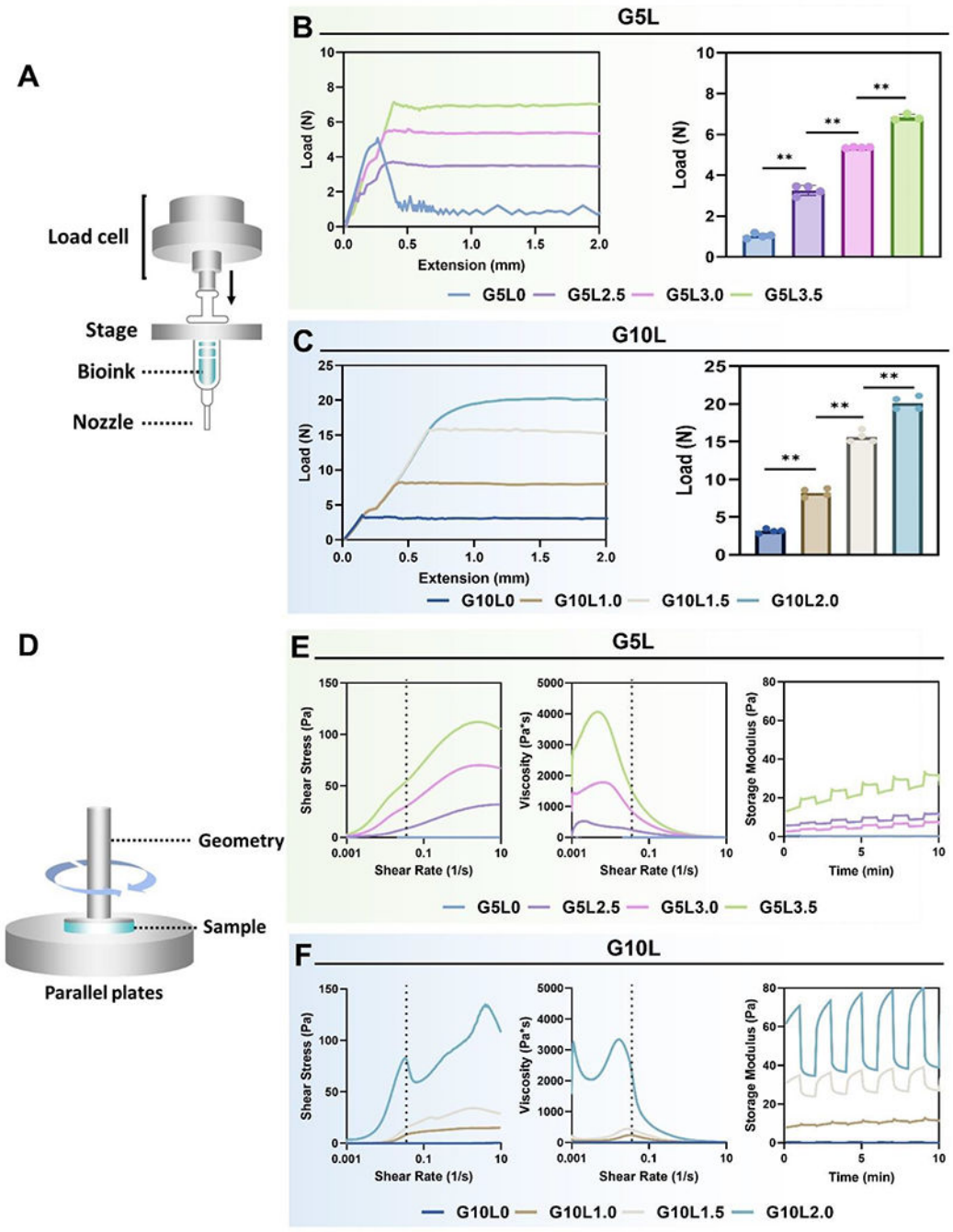

Figure 3. Injection force and rheological characterization.

A) Schematic of injection force measurement setup. B, C) Injection force profile (left) and mean injection force (right) from various GelMA/Laponite hydrogels with a 30G PTFE nozzle/3cc syringe combination (*$p < 0.05$, **$p < 0.01$). D) Schematic illustration of rheological evaluation. E, F) Assessment of rheological parameters including shear stress (left), viscosity (mid), and storage modulus (G′) (right) from various GelMA/Laponite hydrogels.

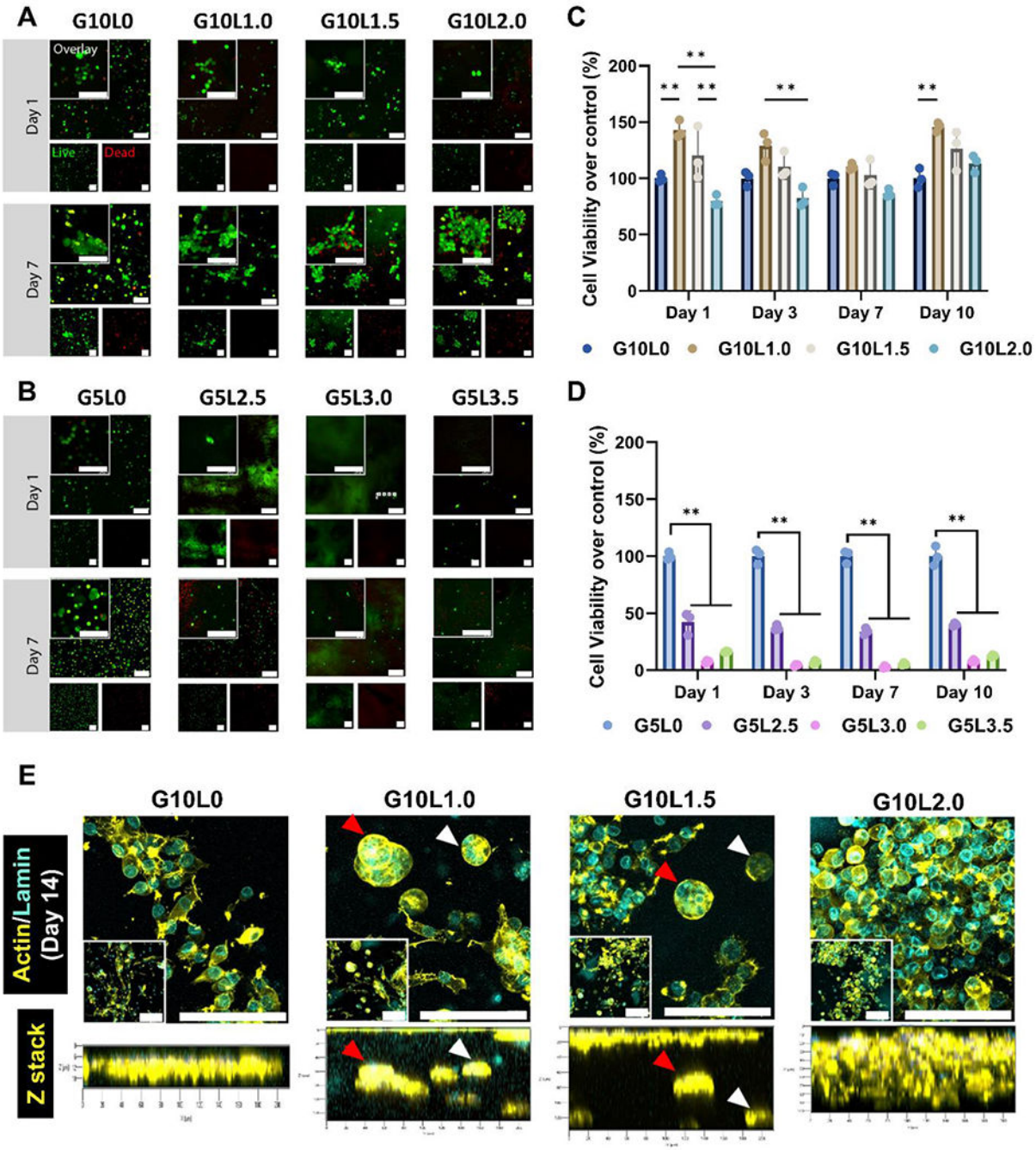

Figure 4. *In vitro* biocompatibility of cell-laden GelMA/Laponite composite hydrogels and morphological studies on the encapsulated pancreatic carcinoma cell line.

A-B) Live/Dead fluorescence images from MIA PaCa-2 cells encapsulated in GelMA/Laponite composite hydrogels followed by culturing for 10 days. C-D) Quantitative analysis of cell viability using Prestoblue assay (5% and 10% GelMA without Laponite) (*$p < 0.05$, **$p < 0.01$) Data are means ± SD (n = 3). E) Characterization of the spatial organization of MIA PaCa-2 cells encapsulated within the 10% GelMA/Laponite composite hydrogels. PFA-fixed *in vitro* tissues were stained with Alexa Fluor® 647 Phalloidin to visualize F-actin (yellow) and Anti-Lamin A/C antibody to visualize nuclei (cyan).

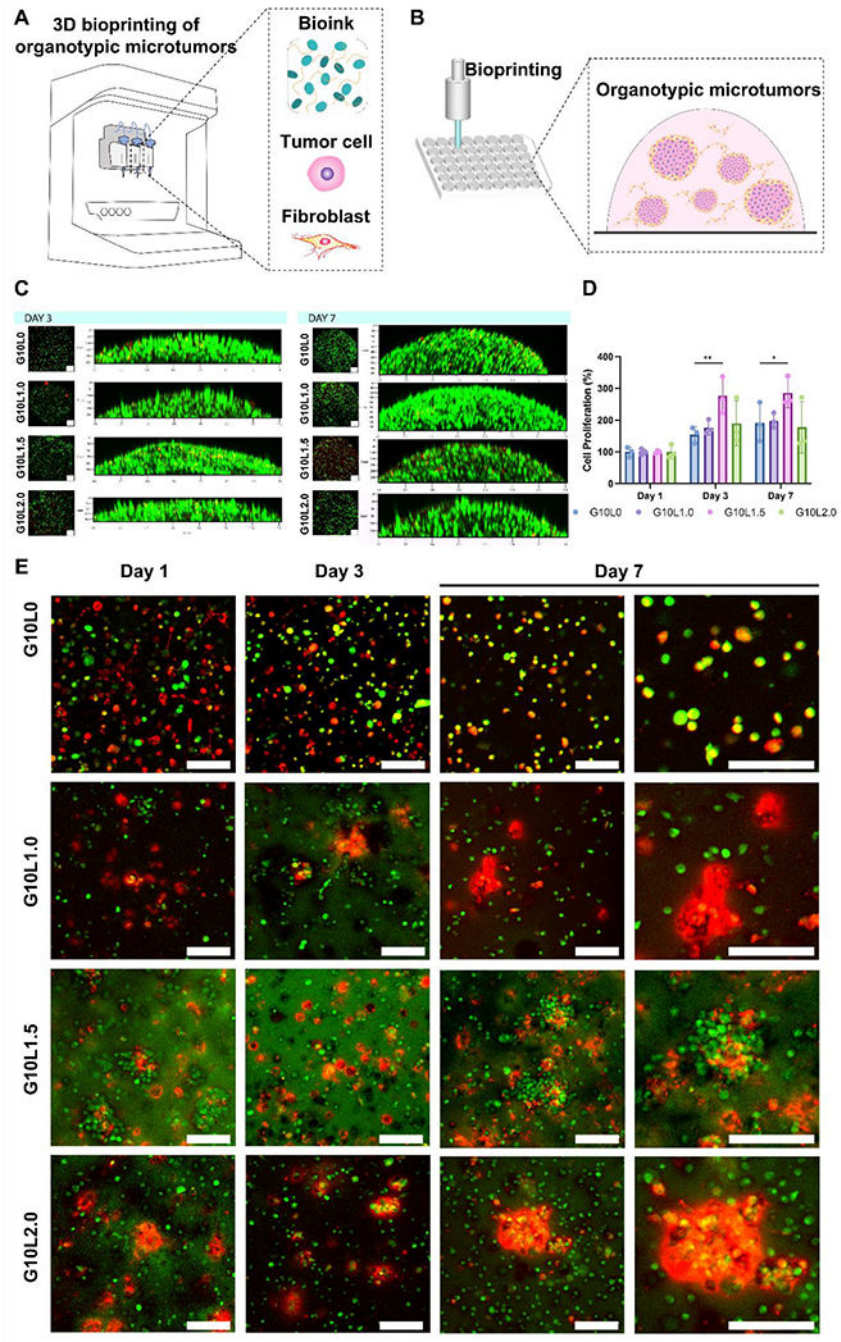

Figure 5. Co-culture *in vitro* biocompatibility and morphological studies on the encapsulated cancer/fibroblast cell lines.

A-B) Schematic representation of 3D bioprinting pancreatic cancer organotypic microtumors employing GelMA/Laponite composite hydrogels. C) Representative image of Live/dead assay. D) Quantitative analysis of cell viability using PrestoBlue assay (*$p < 0.05$, **$p < 0.01$). E) Pancreatic carcinoma cells (MIA PaCa-2) and fibroblasts (C3H10T1/2) were labeled with Live CellTrackers (cancer: green; fibroblast: red), encapsulated in GelMA/Laponite composite hydrogels, and cultured for up to 7 days for evaluating their morphology through confocal images (Scale bar: 100 μm). Data are means ± SD (n = 3).

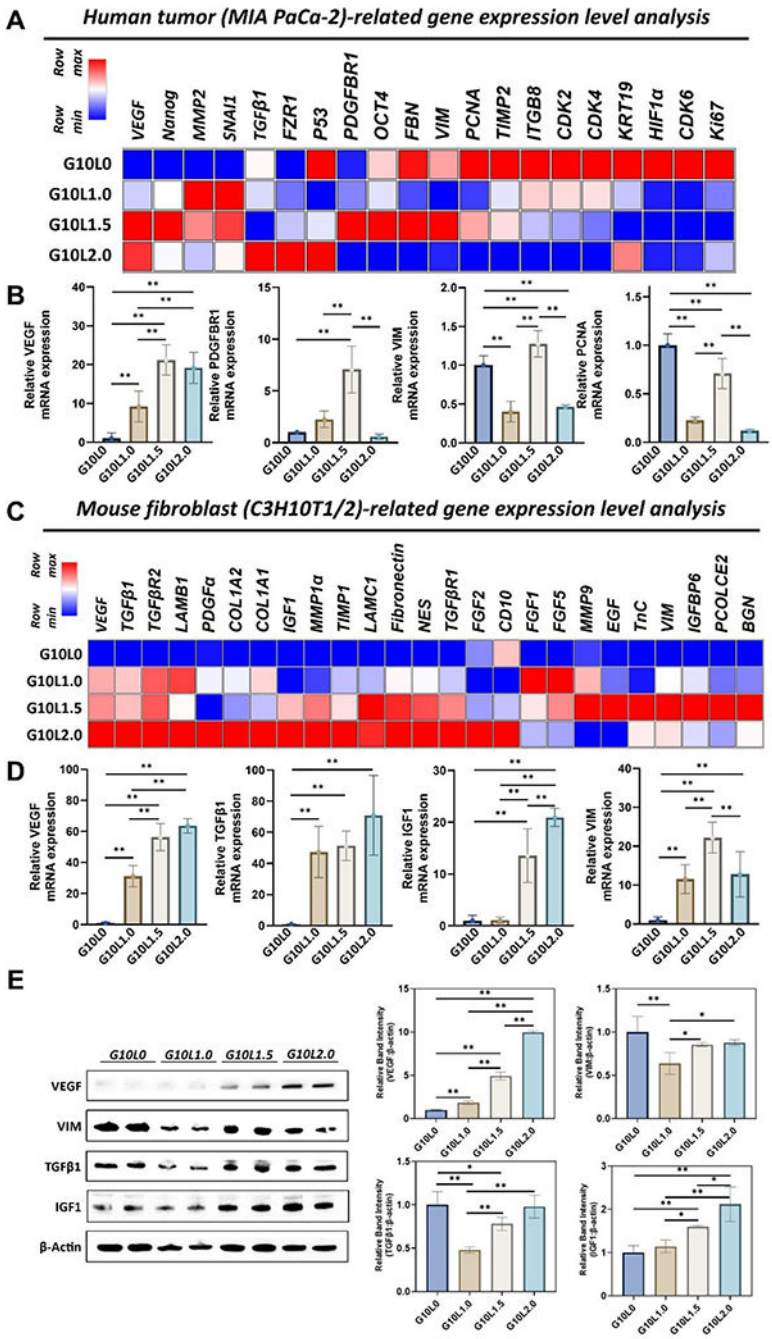

Figure 6.

Gene and protein expression analysis of pancreatic cancer cells (MIA PaCa-2) and embryonic fibroblasts (C3H10T1/2) co-cultured in different GelMA/Laponite composite hydrogels for 3 days. (A) Heatmap analysis of tumoral genes, including growth factor, tissue remodeling, mesenchymal phenotype, stemness, proliferation & cell cycle-related genes. (B) Quantitative analysis of gene expressions. Results are expressed as the mean SD of three replicates of experiments. ($n > 3$, $^{*}p < 0.05$, $^{**}p < 0.01$). (C) Heatmap analysis of mouse fibroblast-related genes, including growth factor, tissue remodeling, ECM,

and mesenchymal phenotype-related genes. (D) Quantitative analysis of gene expressions. Results are expressed as mean ± SD of three replicates of experiments. ($n > 3$, $^{*}p < 0.05$, $^{**}p < 0.01$). (E) Western blotting was used to analyze protein expression levels at different compositions of GelMA/Laponite hydrogels. Quantitative analysis was expressed as mean ± SD. ($n > 3$, $^{*}p < 0.05$, $^{**}p < 0.01$).